

1 **Title: Globally coherent water cycle response to temperature changes during**  
2 **the past two millennia**  
3

4 **Authors:** Bronwen L. Konecky<sup>1\*</sup>, Nicholas P. McKay<sup>2</sup>, Georgina M. Falster<sup>1,3</sup>, Samantha L. Stevenson<sup>4</sup>, Matt J.  
5 Fischer<sup>5</sup>, Alyssa R. Atwood<sup>6</sup>, Diane M. Thompson<sup>7</sup>, Matthew D. Jones<sup>8</sup>, Jonathan J. Tyler<sup>9</sup>, Kristine L. DeLong<sup>10</sup>,  
6 Belen Martrat<sup>11</sup>, Elizabeth K. Thomas<sup>12</sup>, Jessica L. Conroy<sup>13</sup>, Sylvia G. Dee<sup>14</sup>, Lukas Jonkers<sup>15</sup>, Olga V. Churakova  
7 (Sidorova)<sup>16,17</sup>, Zoltán Kern<sup>18,19</sup>, Thomas Opel<sup>20</sup>, Trevor J. Porter<sup>21</sup>, Hussein R. Sayani<sup>22</sup>, Grzegorz Skrzypek<sup>23</sup>, and  
8 Iso2k Project Members<sup>†</sup>  
9

10 **Affiliations:**

11 <sup>1</sup>Department of Earth and Planetary Sciences, Washington University, Saint Louis, Missouri, 63108, USA

12 <sup>2</sup>School of Earth and Sustainability, Northern Arizona University, Flagstaff, AZ, 86011, USA

13 <sup>3</sup>Research School of Earth Sciences and ARC Centre of Excellence for Climate Extremes, Australian National  
14 University, Canberra, ACT, 2601, Australia

15 <sup>4</sup>Bren School of Environmental Science & Management, University of California, Santa Barbara, Santa  
16 Barbara, CA, 93106, USA

17 <sup>5</sup>NSTLI Environment, ANSTO, Sydney, NSW, 2234, Australia

18 <sup>6</sup>Department of Earth, Ocean, and Atmospheric Sciences, Florida State University, Tallahassee, Florida, 32306,  
19 USA

20 <sup>7</sup>Department of Geosciences, University of Arizona, Tucson, Arizona, 85719, USA

21 <sup>8</sup>School of Geography, University of Nottingham, Nottingham, NG7 2RD, UK

22 <sup>9</sup>School of Physics, Chemistry and Earth Sciences, The University of Adelaide, Adelaide, South Australia,  
23 5005, Australia

24 <sup>10</sup>Department of Geography and Anthropology, Coastal Studies Institute, Louisiana State University, Baton  
25 Rouge, LA, 70803, USA

26 <sup>11</sup>Department of Environmental Chemistry, Institute of Environmental Assessment and Water Research  
27 (IDAEA-CSIC), Barcelona, Barcelona, 08034, Spain

28 <sup>12</sup>Department of Geology, University at Buffalo, Buffalo, NY, 14260, USA

29 <sup>13</sup>Department of Geology, Department of Plant Biology, University of Illinois at Urbana-Champaign, Urbana,  
30 IL, 61822, USA

31 <sup>14</sup>Department of Earth, Environmental, and Planetary Sciences., Rice University, Houston, Texas, 77005, USA

32 <sup>15</sup>MARUM Center for Marine Environmental Sciences, Bremen University, Bremen, 28359, Germany

33 <sup>16</sup>Institute of Ecology and Geography, Siberian Federal University, Krasnoyarsk, 660041, Russian Federation

34 <sup>17</sup>Department of Forest Dynamics, Swiss Federal Institute for Forest, Snow and Landscape Research WSL,  
35 Birmensdorf, CH-8903, Switzerland

36 <sup>18</sup>Institute for Geological and Geochemical Research, Research Centre for Astronomy and Earth Sciences,  
37 Eötvös Loránd Research Network, Budapest, H-1112, Hungary

38 <sup>19</sup>CSFK, MTA Centre of Excellence, Budapest, H-1121, Hungary

39 <sup>20</sup>Polar Terrestrial Environmental Systems, Alfred Wegener Institute Helmholtz Centre for Polar and Marine  
40 Research, Potsdam, 14473, Germany

41 <sup>21</sup>Department of Geography, Geomatics and Environment, University of Toronto - Mississauga, Mississauga,  
42 Ontario, L5L1C6, Canada

43 <sup>22</sup>School of Earth and Atmospheric Science, Georgia Institute of Technology, Atlanta, GA, 30332, USA

44 <sup>23</sup>West Australian Biogeochemistry Centre, School of Biological Sciences, The University of Western Australia,  
45 Perth, Western Australia, 6009, Australia  
46  
47  
48

49 † Iso2k Project Members includes all above named authors and: Nerilie J. Abram (Australian National  
50 University, Australia), Kerstin Braun (Arizona State University, USA), Matthieu Carré (Sorbonne Universités  
51 (UPMC)-CNRS-IRD-MNHN, France), Olivier Cartapanis (CEREGE, Aix Marseille Université, CNRS, IRD,  
52 INRAE, France), Laia Comas-Bru (University of Reading, United Kingdom), Mark A. Curran (Australian  
53 Antarctic Division, Australia), Emilie P. Dassié (University of Bordeaux, France), Michael Deininger (Johannes  
54 Gutenberg University Mainz, Germany), Dmitry V. Divine (Norwegian Polar Institute, Norway), Alessandro  
55 Incarbona (Palermo University, Italy), Darrell S. Kaufman (Northern Arizona University, USA), Nikita Kaushal  
56 (University of Oxford, United Kingdom), Robert M. Klaebe (The University of Adelaide, Australia), Hannah R.  
57 Kolus (Northern Arizona University, USA), Guillaume Leduc (Aix Marseille University, CNRS, IRD, INRAE,  
58 Coll France, CEREGE, France), Shreyas R. Managave (Indian Institute of Science Education and Research,  
59 India), P. Graham Mortyn (Universitat Autònoma de Barcelona (UAB), Spain), Andrew D. Moy (Australian  
60 Antarctic Division, Australia), Anais J. Orsi (Laboratoire des Sciences du Climat et de L'Environnement,  
61 France), Judson W. Partin (University of Texas at Austin, USA), Heidi A. Roop (University of Minnesota,  
62 USA), Marie-Alexandrine Sicre (CNRS and Sorbonne Université, France), Lucien von Gunten (PAGES  
63 International Project Office, Switzerland), and Kei Yoshimura (The University of Tokyo, Japan)  
64  
65

66 \* Corresponding author. Email: [bkonecky@wustl.edu](mailto:bkonecky@wustl.edu)  
67  
68

69  
70  
71  
72  
73  
74  
75  
76

77 **The response of the global water cycle to changes in global surface temperature remains an**  
78 **outstanding question in future climate projections and past climate reconstructions. The**  
79 **stable hydrogen and oxygen isotope compositions of precipitation ( $\delta_{\text{precip}}$ ), meteoric water**  
80 **( $\delta_{\text{MW}}$ ), and seawater ( $\delta_{\text{SW}}$ ) integrate processes from microphysical to global scales and thus**  
81 **are uniquely positioned to track global hydroclimate variations. Here, we evaluate global**  
82 **hydroclimate during the past 2,000 years using a globally distributed compilation of**  
83 **proxies for  $\delta_{\text{precip}}$ ,  $\delta_{\text{MW}}$ , and  $\delta_{\text{SW}}$ . We show that global mean surface temperature exerted a**  
84 **coherent influence on global  $\delta_{\text{precip}}$  and  $\delta_{\text{MW}}$  throughout the past two millennia, driven by**  
85 **global ocean evaporation and condensation processes, with lower values during the Little**  
86 **Ice Age (1450-1850) and higher values after the onset of anthropogenic warming (~1850).**  
87 **The Pacific Walker Circulation is a predominant source of regional variability,**  
88 **particularly since 1850. Our results demonstrate rapid adjustments in global precipitation**  
89 **and atmospheric circulation patterns – within decades – as the planet warms and cools.**

90

91 Recent global syntheses of paleoclimate “proxy” data have constrained global mean surface  
92 temperature (GMST) changes during the past 2000 years (i.e., the Common Era, CE), providing  
93 critical context for anthropogenic warming<sup>1,2</sup>. Yet despite the importance of water resources to  
94 society, contemporaneous variations in the global water cycle — including precipitation,  
95 evapotranspiration, atmospheric circulation, and modes of climate variability that affect these  
96 processes — remain underconstrained<sup>3,4</sup>.

97

98 Stable hydrogen and oxygen isotope ratios ( $\delta^2\text{H}$  and  $\delta^{18}\text{O}$ ) in environmental waters are well  
99 positioned to provide a global picture of hydroclimate. Evaporation, condensation, freezing, and

100 other phase changes in the water cycle differentially impact (fractionate) heavy versus light  
101 isotopes, causing the  $\delta^2\text{H}$  and  $\delta^{18}\text{O}$  of precipitation ( $\delta_{\text{precip}}$ ), precipitation-derived meteoric  
102 waters such as lake and soil water ( $\delta_{\text{MW}}$ ), and seawater ( $\delta_{\text{SW}}$ ) to integrate and record hydrological  
103 processes on timescales from minutes to millions of years<sup>5–12</sup>. Variations in  $\delta_{\text{precip}}$ ,  $\delta_{\text{MW}}$ , and  $\delta_{\text{SW}}$   
104 are subsequently incorporated into diverse geologic materials including speleothem and coral  
105 carbonate, glacial ice, and tree cellulose. By synthesizing such data from a variety of sources, it  
106 is therefore possible to infer changes in a powerful suite of hydroclimatic variables:  $\delta_{\text{precip}}$ , which  
107 reflects atmospheric factors such as condensation temperature, precipitation amount, rainout  
108 history, and moisture source<sup>12</sup>;  $\delta_{\text{MW}}$  from lake, soil, and groundwaters, which reflects variations  
109 in  $\delta_{\text{precip}}$  and surface water evaporation; and  $\delta_{\text{SW}}$ , which reflects  $\delta_{\text{precip}}$ , seawater evaporation, and  
110 mixing<sup>13,14</sup>.

111  
112 We analyzed proxies for  $\delta_{\text{precip}}$ ,  $\delta_{\text{MW}}$ , and  $\delta_{\text{SW}}$  from the recently published PAGES Iso2k  
113 database, which contains 759 globally-distributed paleoclimate records from coral, tree, ice,  
114 speleothem, lake, and marine sites<sup>15</sup>. The database includes extensive metadata designed to  
115 facilitate cross-archive comparison, including interpretations from the original publications and  
116 supplemented with information from a team of over 50 archive experts (see ref. <sup>15</sup> for details on  
117 database design). Metadata fields include original climatic interpretations, proxy system  
118 transformations, and the multiple environmental drivers of the isotopic composition of the  
119 measured material in each record (hereafter “isotope interpretation”). Each record is further  
120 classified into one of three primary isotope interpretation groups: 1)  $\delta_{\text{precip}}$ ; 2) Effective Moisture  
121 (EM), i.e., the balance between precipitation and evaporation, with higher EM reflecting higher  
122 precipitation relative to evaporation; or 3) the *in situ* temperature of the environmental medium

123 during the formation of the proxy sensor or archive<sup>15</sup> (we note most records in the temperature  
124 category are marine carbonates whose  $\delta^{18}\text{O}$  primarily reflects seawater temperature, with only  
125 minor influence of  $\delta_{\text{sw}}$ <sup>16</sup>). Regional and global analyses were performed on these three isotope  
126 interpretation groups to distinguish patterns in different reservoirs of the water cycle  
127 (precipitation, surface water, seawater), without *a priori* assumptions about the climatic drivers  
128 of each record's variability (e.g., upstream monsoon intensity, regional air temperature), which  
129 are more subject to change as records are re-interpreted over time (Methods).

130

131 For each group we created composite records of global  $\delta^{18}\text{O}$  anomalies relative to the 0–2000  
132 mean ( $\Delta^{18}\text{O}$ ), including  $\delta^2\text{H}$  records scaled to  $\delta^{18}\text{O}$ -equivalent variance, using a dynamic  
133 compositing method that was previously employed to reconstruct paleotemperature in a manner  
134 that robustly handles proxy timeseries of different lengths, resolutions, and coverage periods (ref.  
135 <sup>17</sup> and Methods). In addition to calculating composites, we performed  
136 Principal Component Analysis (PCA) on a subset of higher-resolution  
137 (i.e.,  $\leq 30$  year bins) individual proxy records with  $>85\%$  temporal data  
138 coverage during the Last Millennium (LM; 850–1850) to reveal  
139 dominant spatiotemporal modes of variability (Methods). We  
140 compared these results to an ensemble of three full-forcing LM  
141 experiments with the water isotope-enabled Community Earth System  
142 Model (iCESM)<sup>18–20</sup>.

143

144 The three  $\Delta^{18}\text{O}$  composites (Fig. 1) display similar patterns, with notable differences in the  
145 magnitude of centennial-scale variability. During the first millennium, composite  $\Delta^{18}\text{O}$  of  $\delta_{\text{precip-}}$   
146 driven records (hereafter, composite  $\Delta^{18}\text{O}_{\delta_{\text{precip}}}$ ) was relatively stable, whereas composite  $\Delta^{18}\text{O}$   
147 of EM- and temperature-driven records (composite  $\Delta^{18}\text{O}_{\text{EM}}$  and  $\Delta^{18}\text{O}_{\text{temp}}$ ) increased and  
148 decreased, respectively. During the LM, all three composites show a monotonic trend from  $\sim 800$   
149 to  $\sim 1700$ , and a reversal of that trend since the 19<sup>th</sup> century. These patterns broadly echo the  
150 temporal evolution of GMST during the LM<sup>1</sup>, but with different magnitudes depending on the  
151 primary environmental interpretation of  $\delta^{18}\text{O}$ . From 1000 to 1850, a global cooling of  $0.25 (\pm \mp$   
152  $0.1)^\circ\text{C}^{-1}$  corresponds to a change of  $-0.27 (\pm 0.00021)$ ,  $+0.02 (\pm 0.00019)$ ,  
153 and  $+0.09\% (\pm 0.0002)$  in composite  $\Delta^{18}\text{O}_{\delta_{\text{precip}}}$ ,  $\Delta^{18}\text{O}_{\text{EM}}$ , and  $\Delta^{18}\text{O}_{\text{temp}}$ ,  
154 respectively (Fig. 1A–C). Subsequent warming of  $0.65 (\pm 0.06)^\circ\text{C}$  from  
155 1850 to 2000 corresponds to a change of  $+0.56 (\pm 0.00012)$ ,  $+0.62 (\pm$   
156  $0.00017)$ , and  $-0.16\% (\pm 0.00023)$ , respectively. Uncertainties in these estimates  
157 are based on differences between the respective time periods across the full ensemble (Methods).  
158  
159 Composite  $\Delta^{18}\text{O}_{\text{EM}}$  displays pronounced centennial-scale variability, with distinct positive  
160 excursions from 300–500, 700–900, and 1800–2000. Variability in composite  $\Delta^{18}\text{O}_{\text{EM}}$  is at least  
161 twice the magnitude of composite  $\Delta^{18}\text{O}_{\text{temp}}$  or  $\Delta^{18}\text{O}_{\delta_{\text{precip}}}$  (Fig. 1), likely due to the strong  
162 influence of surface-water evaporation on lake and seawater  $\delta^{18}\text{O}$ , which amplifies the  $\delta_{\text{precip}}$   
163 signal relative to noise<sup>11,12</sup>.  
164  
165 The first principal component (PC1) of each category of records is dominated by a monotonic  
166 trend over the LM, with smaller centennial-scale fluctuations (Fig. 2A). Similar to the

167 composites, the gross trend in each PC1 corresponds to a decrease in GMST. Site loadings on  
168 each PC1, however, differ by region and by the primary environmental driver of  $\delta^{18}\text{O}$  (Fig. 2B-  
169 D). For example, positive trends and negative PC1 loadings are evident in  $\delta^{18}\text{O}_{\text{temp}}$  at almost all  
170 extra-tropical locations (Fig. 2D), consistent with the impact of ocean cooling on the  $\delta^{18}\text{O}$  of  
171 marine carbonates. Contrastingly, trends are insignificant in the Indo-Pacific Warm Pool where  
172  $\delta^{18}\text{O}_{\text{sw}}$  influence likely confounds the temperature signal<sup>21</sup>.

173

#### 174 **Influence of temperature on global $\delta_{\text{MW}}$**

175 Together, the  $\Delta^{18}\text{O}$  composites and PC1 suggest that GMST exerts a first-order control on  
176 temporal changes in global  $\delta_{\text{MW}}$  during the CE. The relationship of composite  $\Delta^{18}\text{O}_{\delta_{\text{precip}}}$  with  
177 temperature is  $0.68 \pm 0.20 \text{‰}/^\circ\text{C}$  for the full CE and  $0.78 \pm 0.19 \text{‰}/^\circ\text{C}$  from 850-2000, based on  
178 regression of the 30-year binned values (Methods) (Fig. 1A). A positive relationship between  
179 GMST and  $\delta_{\text{precip}}$  may be expected from high latitude ice cores<sup>12,22,23</sup>, but positive relationships in  
180 composite  $\Delta^{18}\text{O}_{\delta_{\text{precip}}}$  persist even when such records are excluded (Extended Data Fig. 1), and  
181 also occur at mid and low latitudes, especially after 1850 (Extended Data Fig. 2). In addition to  
182 the composites, the positive relationship between  $\delta_{\text{precip}}$  and GMST is evident in PC1 of the  $\delta_{\text{precip}}$   
183 records spanning the entire CE (Extended Data Fig. 3A-B) and in iCESM simulations (Fig.  
184 3A,D; Extended Data Fig. 4). In iCESM, the regression slope between GMST and global, 30-  
185 year smoothed, mean annual  $\delta^{18}\text{O}_{\text{precip}}$  from 850-2000 is  $0.25\text{‰}/^\circ\text{C}$ , and  $0.48\text{‰}/^\circ\text{C}$  when  
186 calculated using Iso2k site locations (which, for  $\delta_{\text{precip}}$  records, excludes nearly all ocean grid  
187 cells and regions where site-level regression slopes are close to 0; Extended Data Fig. 4). The  
188 iCESM slopes are shallower than in the Iso2k data, but the global slope is consistent with earlier  
189 GCM estimates of  $0.3\text{‰}/^\circ\text{C}$  during the last deglaciation<sup>24</sup> and simplified model estimates of

190 zonal-mean temporal slopes of  $\sim 0.1\text{--}0.4\text{‰}/^\circ\text{C}$  for most latitudes<sup>25</sup>. The discrepancy between the  
191 Iso2k and iCESM temporal slopes may reflect model biases in extratropical moisture transport  
192 and positive  $\delta^{18}\text{O}_{\text{precip}}$  biases at the high latitudes<sup>18</sup>. However, the global temporal slope between  
193 GMST and  $\delta^{18}\text{O}_{\text{precip}}$  has not been quantified observationally— unlike spatially-derived slopes  
194 between site-level air temperature and  $\delta^{18}\text{O}_{\text{precip}}$ <sup>11,12,22</sup>— because modern  $\delta^{18}\text{O}_{\text{precip}}$  measurements  
195 in most regions are either absent or too short and discontinuous (most records  $<10$  years) to do so  
196 beyond the scale of a few years<sup>26,27</sup>. Despite differences in magnitude, both iCESM and Iso2k  
197 data demonstrate that a positive relationship between GMST and  $\delta_{\text{MW}}$  is a persistent feature of  
198 the global water cycle for the CE. The 30-year-binned Iso2k temporal slope of  $0.68 \pm 0.20 \text{‰}/^\circ\text{C}$   
199 should be considered a benchmark to be tested as longer observations and reanalyses become  
200 available.

201  
202 Ice core and marine sediment studies have long recognized the importance of air temperature in  
203 driving high latitude  $\delta_{\text{MW}}$ , and of global ice volume in driving global  $\delta_{\text{SW}}$ , on glacial-interglacial  
204 timescales and across the Cenozoic<sup>12,23</sup>. However, the nature of this relationship has remained  
205 uncertain on the shorter (decadal to centennial) timescales most relevant for understanding  
206 modern climate change and its impacts on water resources. Our results provide the first  
207 observational evidence that GMST drives temporal changes in  $\delta_{\text{MW}}$  and  $\delta_{\text{SW}}$ , and therefore  
208 changes in the hydrological cycle, on such timescales. Mechanisms other than global ice volume,  
209 which has not changed substantially during the CE, are therefore required to explain this  
210 relationship.

211



212 Although the Iso2k analyses are the first to document it, stable isotope theory and experimental  
213 studies provide ample foundation for a positive imprint of GMST on global  $\delta_{\text{MW}}$ , which is what  
214 our spatially-distributed (albeit not spatially continuous) proxy network approximates. At the  
215 global scale, a relationship between  $\delta_{\text{MW}}$  and GMST will integrate all processes that relate local-  
216 scale  $\delta_{\text{MW}}$  with GMST, while balancing out regional distributions of heavy vs. light  
217 isotopologues throughout the water cycle. Variations in global  $\delta_{\text{MW}}$  therefore reflect variations in  
218 the isotopic composition of the global oceanic and atmospheric reservoirs. Atmospheric  $\delta_{\text{vapor}}$  is  
219 ultimately governed by the isotopic composition of water evaporated from the oceans.  
220 Equilibrium fractionation is greater at lower temperatures<sup>12,28</sup>, so in a cooler world, the liquid-to-  
221 vapor difference in  $\delta^{18}\text{O}$  is higher than in warmer conditions (i.e., lower  $\delta_{\text{vapor}}$  in the saturated  
222 atmospheric layer above the ocean surface). Kinetic fractionation further decreases atmospheric  
223  $\delta_{\text{vapor}}$  as newly evaporated vapor diffuses and mixes into the undersaturated free atmosphere,  
224 with stronger fractionation when the lower troposphere is less humid<sup>29,30</sup>. A globally cooler and  
225 drier troposphere should therefore decrease  $\delta_{\text{vapor}}$  to a greater extent than a warmer and more  
226 humid troposphere. Global  $\delta_{\text{vapor}}$  is further modified by temperature-dependent fractionation as  
227 precipitation forms and condensation preferentially removes  $^{18}\text{O}$  and decreases  $\delta_{\text{vapor}}$ , with  
228 greater isotopic discrimination at colder condensation temperatures<sup>12,28</sup>.  
229  
230 iCESM simulations indicate multiple mechanisms play a role (Fig. 3). Higher GMST is  
231 associated with higher  $\delta^{18}\text{O}$  of water vapor flux from evaporating seawater into the saturated  
232 boundary layer (0.14‰/°C), following the Craig-Gordon model<sup>13,31</sup>, slightly higher relative  
233 humidity with respect to sea surface temperature (0.77‰/°C) (Methods), and ultimately, higher  
234 atmospheric  $\delta^{18}\text{O}_{\text{vapor}}$  (0.30‰/°C). Global  $\delta_{\text{precip}}$  therefore reflects not only the  $\delta_{\text{vapor}}$  determined

235 during ocean evaporation and mixing into the free atmosphere, but also the subsequent depletion  
236 of  $^{18}\text{O}$  in atmospheric vapor in the atmosphere through condensation, which via equilibrium  
237 fractionation is stronger in a cooler climate. Stronger depletion of heavy isotopes in precipitation  
238 also occurs with more vigorous circulation and shorter residence time of atmospheric moisture<sup>32</sup>.  
239 For precipitation integrated over the timescales of most proxy systems (weeks to months),  $\delta_{\text{precip}}$   
240 could become even lower when global precipitation rates are high relative to the amount of  
241 precipitable water in the atmosphere, and higher when atmospheric humidity increases to a  
242 greater extent than precipitation rate, as in the 20th century (Fig. 3; ref. <sup>33</sup>).

243  
244 Theory and simplified model experiments suggest that a cooler global atmosphere could also  
245 favor stronger latitudinal gradients in  $\delta_{\text{precip}}$ <sup>12</sup>, as lower temperatures increase distillation along  
246 the water's path from the subtropics to the poles<sup>22,34</sup>. A cooler atmosphere may also shift  
247 evaporative source regions equatorward, driving a greater fraction of high latitude precipitation  
248 to be sourced remotely<sup>25</sup> which strongly affects  $\delta_{\text{precip}}$  at those latitudes<sup>35</sup>. The latitudinal gradient  
249 in Iso2k  $\delta_{\text{precip}}$  records between 40° to 70° N and S is approximately -0.48‰ per degree latitude,  
250 in agreement with observed modern slopes of ~ -0.3 to -0.6‰ per degree latitude<sup>22,34</sup>. However,  
251 we observe no difference in this gradient between the Little Ice Age and the 20th century — the  
252 globally coldest and warmest intervals of the CE, respectively<sup>1,36</sup> (Extended Data Fig. 5). Hence,  
253 either equator-to-pole Rayleigh distillation is counterbalanced by changes in spatial patterns of  
254 global evaporative recharge and moisture transport relative to precipitation<sup>25,35</sup>, or the spread in  
255 Iso2k  $\delta_{\text{precip}}$  records is too large to resolve changing gradients during the LM when temperature  
256 changes are relatively small. As spatial gradients are averaged out at the global scale, further  
257 experiments with both simplified models and isotope-enabled GCMs are needed to quantitatively

258 decompose the relative importance of ocean evaporation, condensation, and global precipitation  
259 and evaporation patterns on the global-scale GMST-  $\delta_{\text{precip}}$  relationship.

260

### 261 **Patterns of regional variability**

262 Despite its influence on global mean  $\delta_{\text{MW}}$ , GMST explains neither the spatial patterns nor the  
263 shorter-term variability in  $\delta_{\text{MW}}$  and  $\delta_{\text{SW}}$  (Fig. 2, Extended Data Fig. 6). Instead, site-level PC1  
264 loadings, LM trends, and centennial anomalies in  $\delta^{18}\text{O}_{\delta_{\text{precip}}}$  and  $\delta^{18}\text{O}_{\text{EM}}$  are spatially  
265 heterogeneous (Figs. 1-2, Extended Data Fig. 7). Although non-climatic processes and noise  
266 likely contribute to this variability, this result also indicates that regional water balance,  
267 atmospheric circulation, and precipitation characteristics dominate regional  $\delta_{\text{MW}}$  not just in the  
268 late 20th/early 21st centuries<sup>26,27</sup> but also on multi-decadal to millennium-long timescales. In the  
269 Arctic and the tropical Andes, negative trends in  $\delta^{18}\text{O}_{\delta_{\text{precip}}}$  and positive PC1 loadings agree with  
270 documented Little Ice Age climate changes: high-latitude cooling, which lowered  $\delta_{\text{precip}}$  in the  
271 Arctic<sup>37</sup>, and intensification of the South American summer monsoon, which lowered  $\delta_{\text{precip}}$  in  
272 the Andes<sup>38</sup>. In eastern China and the Maritime Continent, positive PC1 loadings and negative  
273 trends in  $\delta^{18}\text{O}_{\delta_{\text{precip}}}$  and  $\delta^{18}\text{O}_{\text{EM}}$  over the LM indicate increasing effective moisture, with  
274 depletion of heavy isotopes at some sites enhanced by intensifying convection and moisture  
275 transport within the East Asian and Australasian summer monsoons<sup>39,40</sup>. In northwestern North  
276 America and Central America, negative PC1 loadings and positive trends in  $\delta^{18}\text{O}_{\delta_{\text{precip}}}$  and  
277  $\delta^{18}\text{O}_{\text{EM}}$  indicate increasing  $\delta^{18}\text{O}_{\text{MW}}$  and declining EM over the LM, while southwestern North  
278 America shows the opposite pattern, consistent with other LM proxy reconstructions<sup>41,42</sup>.  $\delta^{18}\text{O}_{\text{EM}}$   
279 from lakes exhibit the clearest trends in western North America, likely because  $\delta_{\text{precip}}$  in the  
280 western North American interior is especially sensitive to changes in water balance<sup>27</sup> and

281 enhanced evaporation during dry periods then amplifies increases in lake water  $\delta^{18}\text{O}$ . This  
282 explains why coherent patterns emerge in western North American isotopic proxy records  
283 despite substantial heterogeneity in compilations that blend isotopic and non-isotopic records<sup>42</sup>.  
284

285 Opposing precipitation anomalies between southwestern North America and Central Asia versus  
286 the Maritime Continent and South Asia during the LM have previously been attributed to  
287 variability in the El Niño-Southern Oscillation<sup>43</sup>, the interannual component of the east-west  
288 atmospheric overturning circulation over the tropical Pacific known as the Pacific Walker  
289 Circulation (PWC)<sup>44</sup>. An underlying influence of the PWC may also explain some of the regional  
290 coherency in Iso2k  $\delta_{\text{MW}}$ . In modern precipitation, strengthening and weakening of the PWC  
291 drives opposing precipitation and  $\delta^{18}\text{O}_{\text{precip}}$  anomalies in Asia and the Americas due to changes  
292 in precipitation amount, moisture source, and transport pathways<sup>26</sup>. For example, rerouting of the  
293 jet stream during El Niño events alters Pacific Ocean moisture trajectories toward southwestern  
294 rather than northwestern North America<sup>45,46</sup>. To the extent that these relationships persist beyond  
295 interannual timescales, changes in moisture transport and EM provide a plausible mechanism for  
296 multidecadal to centennial patterns in Asian and western North American  $\delta^{18}\text{O}_{\text{EM}}$ .  
297

298 Evidence for the PWC's influence on Iso2k records is stronger on sub-decadal timescales during  
299 the historical period (1850–2005), when instrumental observations are available for direct  
300 comparison. We correlated PC1 of 3-year binned Iso2k EM records with observed sea level  
301 pressure (SLP) and found that the associated pattern mimics the observed global expression of  
302 the PWC (Fig. 4a). Similarly, in iCESM experiments, PC1 of soil water  $\delta^{18}\text{O}$  ( $\delta^{18}\text{O}_{\text{soil}}$ ) at Iso2k  
303 EM sites displays an SLP pattern that resembles iCESM's PWC (Fig. 4b). There is vigorous

304 debate surrounding the extent to which the PWC fluctuates on multidecadal and longer  
305 timescales, either due to internal variability in the climate system or to external forcing<sup>47-50</sup>. Our  
306 results suggest that the PWC was the predominant influence on interannual  $\delta^{18}\text{O}_{\text{precip}}$  not only  
307 from 1982 to 2015<sup>26</sup>, but at least since 1850, and likely on multi-decadal timescales prior to  
308 1850.

309  
310 Our results reveal a remarkably consistent relationship between GMST and  $\delta_{\text{MW}}$  throughout the  
311 CE, despite relatively constant ice-ocean boundary conditions. Between 1850-2000, global  $\delta_{\text{precip}}$   
312 increased by at least 0.56‰, indicative of a warmer, more humid troposphere. Global  $\delta_{\text{MW}}$  and  
313 regional  $\delta_{\text{MW}}$  appear to adjust to changing temperature and atmospheric circulation patterns,  
314 respectively, within decades – similar to the timescale of the forcing itself. Expanded  $\delta_{\text{MW}}$   
315 observational networks are critical for detecting and attributing shifts in rainfall, drought, and  
316 circulation as the planet continues to warm.

317

### 318 **Acknowledgments**

319 Iso2k is a contribution to Phase 3 and 4 of the PAGES 2k Network. PAGES received support  
320 from the Swiss Academy of Sciences, the US National Science Foundation, and the Chinese  
321 Academy of Sciences. We thank three anonymous reviewers for helpful comments which  
322 improved this manuscript.

323

324 Support for this work includes NSF-AGS 1805141, NSF-AGS PRF 1433408, and a David and  
325 Lucile Packard Foundation Fellowship in Science and Engineering to BLK; NSF-1948746 to  
326 NPM; Australian Research Council through a Discovery Project (DP170100557) and the Centre

327 of Excellence for Climate Extremes (CE170100023) to GMF; NSF-AGS 1805143 and NSF-  
328 OCE-2202794 to SLS; NSF-CAREER 2145725, NSF 2103035, and NSF 2002444 to ARA;  
329 NSF-CAREER 1945479, NSF 1931242, and NSF 2002460 to DMT; Australian Research  
330 Council Discovery Project DP190102782 to JJT; South Central Climate Adaptation Science  
331 Center Cooperative Agreement G19AC00086, NSF-2102931, and NSF-1805702 to KLD; RYC-  
332 2013-14073 programme and LINKA20102 and CEX2018-000794-S projects to BM; NSF-EAR  
333 PRF 1349595, NSF-EAR-IF 1652274, NSF-OPP 1504267, NSF-OPP 1737716, and NSF-  
334 CAREER 2044616 to EKT; NSF-CAREER 1847791 to JLC; NOAA Award Number  
335 NA18OAR4310427 to SGD; PalMod, the German paleoclimate modeling initiative, part of the  
336 Research for Sustainable Development initiative funded by the German Federal Ministry of  
337 Education and Research (BMBF; 01LP1922A) to LJ; RSF project 21-17-00006 to OVC(S);  
338 German Research Foundation grants OP217/2-1, OP217/3-1, OP217/4-1 to TO; Natural Sciences  
339 and Engineering Research Council of Canada Discovery Grant RGPIN-2016-06730 to TJP;  
340 Australian Research Council Project (LP210300691) to GS; Australian Research Council  
341 through a Future Fellowship (FT160100029), Special Research Initiative for the Australian  
342 Centre for Excellence in Antarctic Science (SR200100008) and the Centre of Excellence for  
343 Climate Extremes (CE170100023) to NJA.

344

345 **Author contributions**

346

347 Analyses presented in the main text and extended data were conceived and performed by BLK,  
348 NPM, GMF, SS, MJF, AA, DMT, MDJ, JJT, EKT, JLC, SGD, and LJ.

349

350 Results were analyzed and interpreted by BLK, NPM, GMF, SS, MJF, AA, DMT, MDJ, KLD,  
351 JJT, BM, and EKT, with input from all authors.

352

353 The manuscript was written mainly by BLK, NPM, GMF, SS, MJF, AA, DMT, MDJ, KLD, JJT,  
354 BM, EKT, JLC, SGD, LJ, and HRS, with additional contributions from OVC, ZK, TO, TJP, and  
355 GS.

356

357 All Iso2k Project Members created the Iso2k database and edited the manuscript.

358

359 BLK directed the project, led the overall design of the study, and led the writing of the  
360 manuscript.

361

362 **Competing interests:**

363

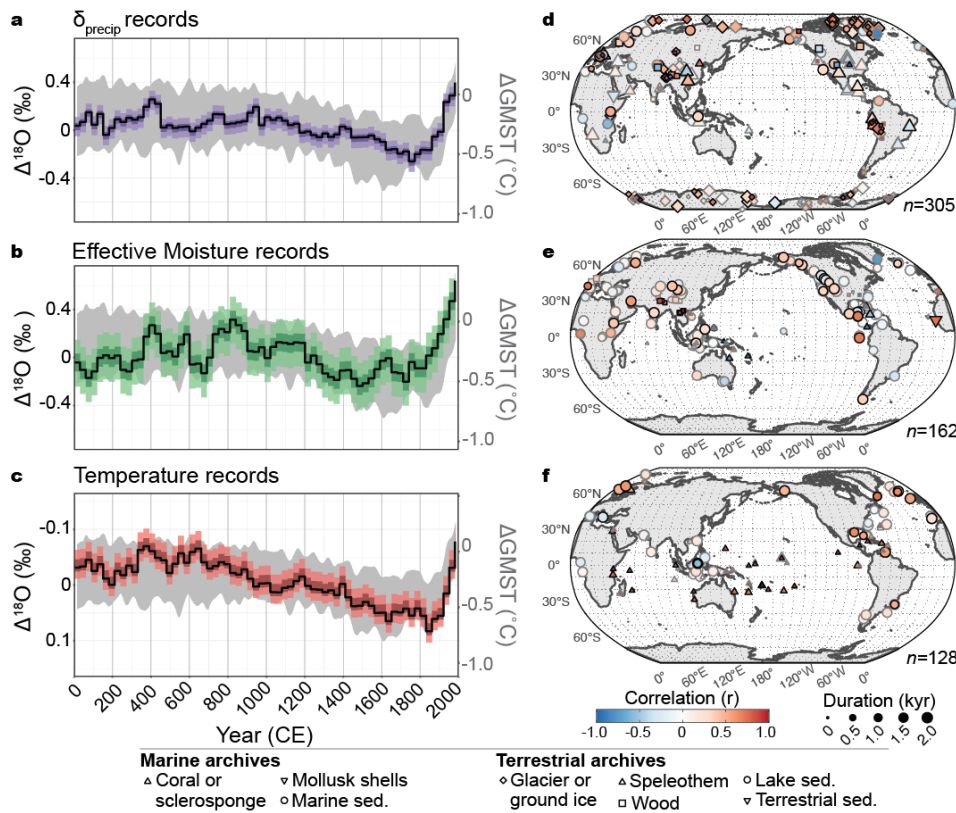
364 The authors declare no competing interests.

365

366

367 **Figure legends/captions**

368



369

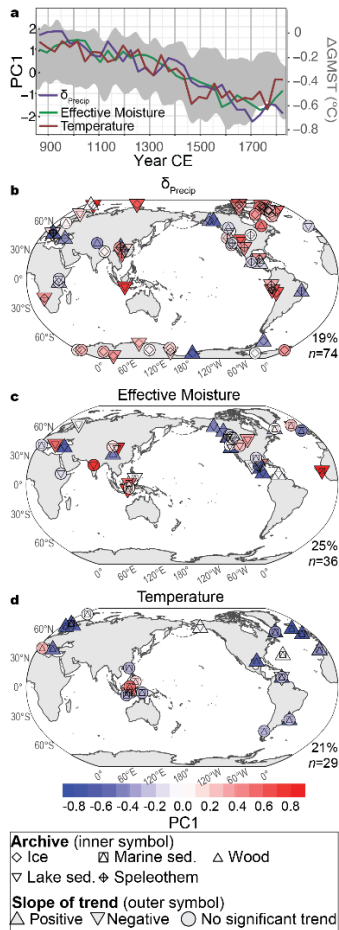
370 **Fig. 1. Global composite  $\delta^{18}\text{O}$  anomalies.** **a-c**, 30-year binned proxy  $\Delta^{18}\text{O}$  (black line, ensemble  
 371 median; dark shading, 25<sup>th</sup>–75<sup>th</sup> percentiles; light shading, 2.5<sup>th</sup>–97.5<sup>th</sup> percentiles) for each group  
 372 of Iso2k records<sup>15</sup>, anomalies relative to 2000-year mean. Gray shading depicts ensemble 2.5<sup>th</sup>–  
 373 97.5<sup>th</sup> percentile GMST anomaly relative to 1961–1990 mean<sup>1</sup>. Note y-axis in (c) is reversed to  
 374 orient values upwards for warmer periods. **d-f**, Records contributing to each composite. Symbol  
 375 shape, archive type; size, record duration; shading, correlation between that record and the  
 376 corresponding composite; bold outline,  $p < 0.05$ . Correlations are Pearson’s  $r$ , two-sided, with no  
 377 adjustment for multiple correlation. Maps created in R, using coastlines from Natural Earth.

378

379



380



381

382 **Fig. 2. First principal components and trends in Iso2k records over the Last Millennium. a,**

383 PC1 of 30-year binned Iso2k<sup>15</sup> records (850 to 1840), by interpretation group (colored lines),

384 compared to GMST anomaly (gray shading) as in Fig. 1. **b-d**, Spatial loadings on PC1 (symbol

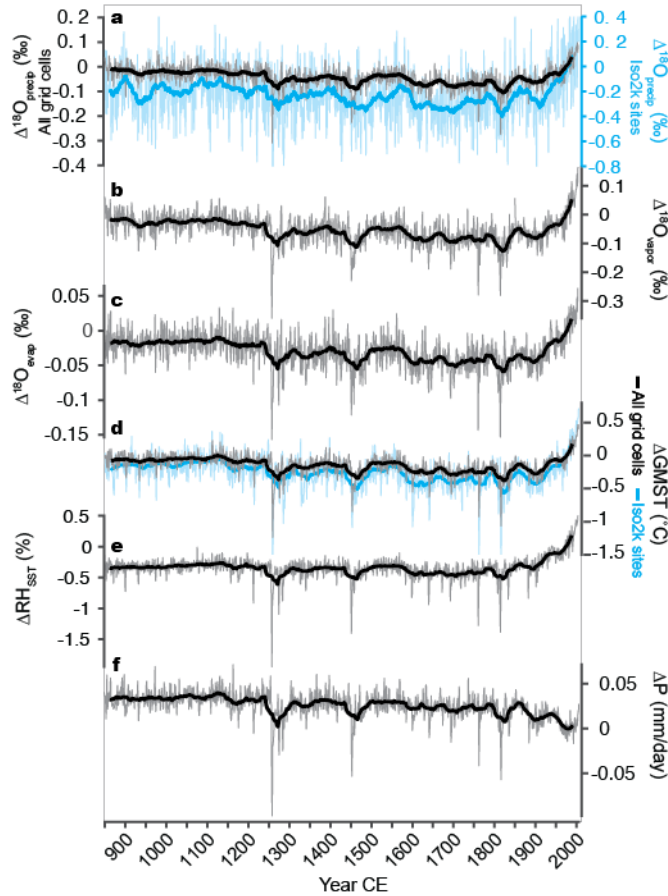
385 shading) for each group. Correlations are Pearson's r, two-sided, with no adjustment for multiple

386 correlation. Inner symbols, archive type; outer symbol shape, slope of significant ( $p < 0.05$ ) linear

387 trend in the  $\delta^{18}O$  of each individual record; labels, variance explained by PC1 and number of

388 records used. Maps created in R, using coastlines from Natural Earth.

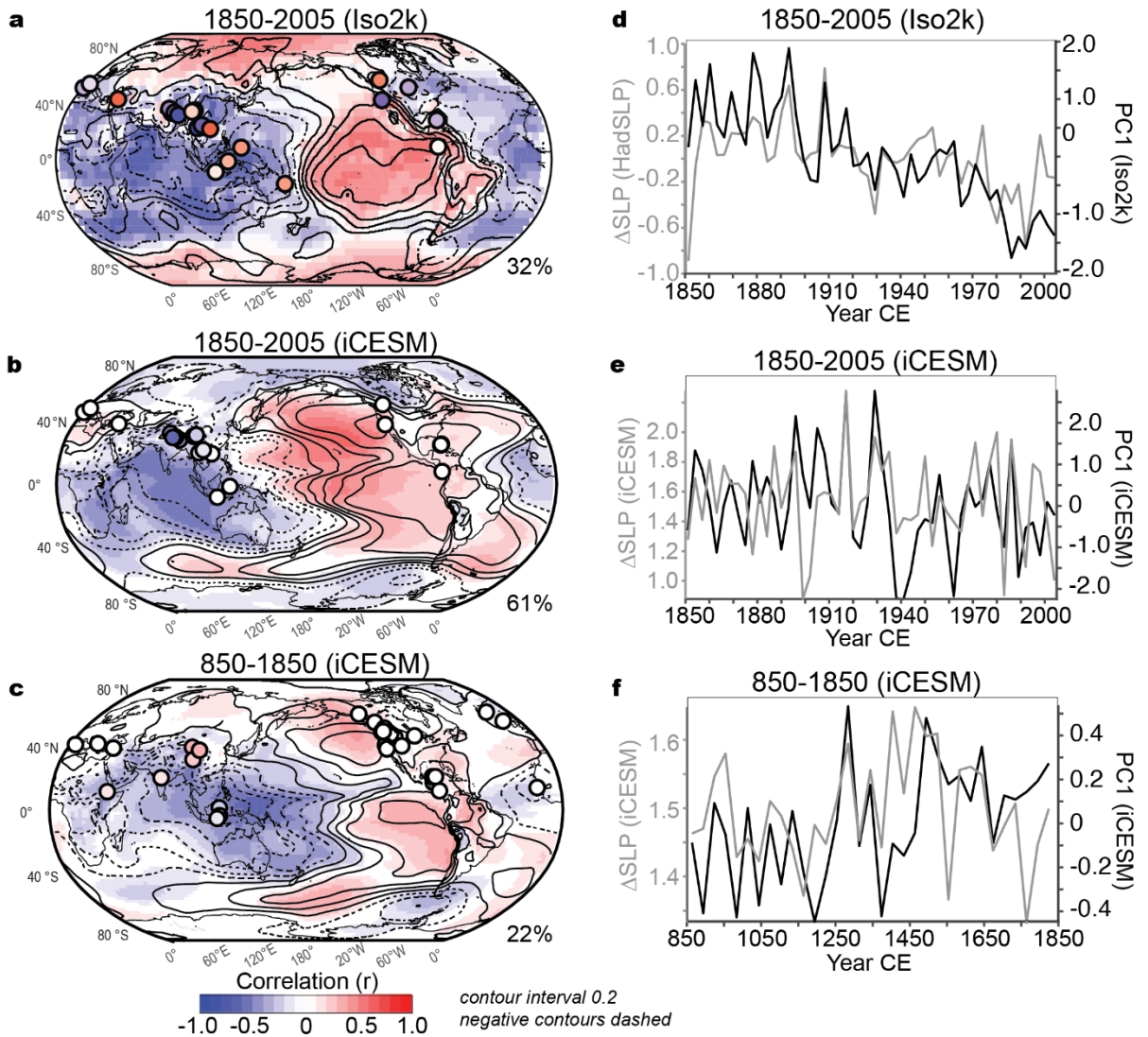
389



390

391 **Fig. 3. Global hydroclimate and isotopic anomalies in iCESM<sup>18-20</sup>.** **a**, Ensemble mean,  
 392 amount-weighted mean annual  $\Delta^{18}\text{O}_{\text{precip}}$  anomaly relative to 1961 to 1990 mean (thin gray line)  
 393 and 30-year running mean (thick black line) for all grid cells, and for only grid cells containing  
 394 Iso2k site locations (blue lines). Note right Y axis in a is scaled 2x that of the left. **b-f**, as in **a**,  
 395 but for **(b)** global column-averaged  $\Delta^{18}\text{O}_{\text{vapor}}$ , **(c)**  $\Delta^{18}\text{O}$  of evaporative flux from the global  
 396 oceans, **(d)** GMST, **(e)** relative humidity over the low- and mid-latitude oceans ( $60^{\circ}\text{N}$ - $60^{\circ}\text{S}$ ),  
 397 with respect to saturation vapor pressure at sea surface temperature<sup>13,29,30</sup>, and **(f)** global  
 398 precipitation rate.

399



400

401 **Fig. 4. Isotopic fingerprint of the Pacific Walker Circulation in Iso2k<sup>15</sup> and iCESM<sup>18-20</sup>.** **a,**

402 Shading is the correlation between observed SLP and PC1 of 3-year binned Iso2k EM records

403 (1850 to 2005). Symbol colors denote site loading on PC1. Unfilled contours denote correlation

404 between SLP and PWC index  $\Delta$ SLP. **b,** Correlation between SLP and ensemble-mean PC1 of 3-

405 year binned 0-10 cm  $\delta^{18}\text{O}_{\text{soil}}$  in iCESM experiments (1850 to 2005), using grid cells of Iso2k EM

406 sites (symbols). **c,** As in **b,** but for 30-year binned data from 850-1850. **d-f,** Time series of PC1

407 (black line) and  $\Delta$ SLP (gray line) corresponding to panels **a-c**. Maps created in MATLAB using

408 `m_map` for coastlines.

409

410

411 **References**

412

- 413 1. PAGES 2k Consortium. Consistent multidecadal variability in global temperature reconstructions  
414 and simulations over the Common Era. *Nature Geoscience* **12**, 643–649 (2019).
- 415 2. PAGES 2k Consortium. A global multiproxy database for temperature reconstructions of the  
416 Common Era. *Sci Data* **4**, 170088 (2017).
- 417 3. Field, C. B. *et al.* Part A: Global and sectoral aspects. Contribution of Working Group II to the Fifth  
418 Assessment Report of the Intergovernmental Panel on Climate Change. in *Climate Change 2014:*  
419 *Impacts, Adaptation, and Vulnerability* (Cambridge University Press, 2014).
- 420 4. Smerdon, J. E. *et al.* Comparing proxy and model estimates of hydroclimate variability and change  
421 over the Common Era. *Proxy Use-Development-Validation/Terrestrial Archives/Centennial-Decadal*  
422 (2017) doi:10.5194/cp-2017-37-RC1.
- 423 5. Rozanski, K. Isotopes in Atmospheric Moisture. in *Isotopes in the Water Cycle* (eds. Aggarwal, P.  
424 K., Gat, J. R. & Froehlich, K. F.) 291–302 (Springer, 2005).
- 425 6. Galewsky, J. *et al.* Stable isotopes in atmospheric water vapor and applications to the hydrologic  
426 cycle. *Reviews of Geophysics* **54**, 809–865 (2016).
- 427 7. Konecky, B. L., Noone, D. C. & Cobb, K. M. The Influence of Competing Hydroclimate Processes  
428 on Stable Isotope Ratios in Tropical Rainfall. *Geophys. Res. Lett.* **46**, 1622–1633 (2019).
- 429 8. Jasechko, S. Global isotope hydrogeology—review. *Rev. Geophys.* **57**, 835–965 (2019).
- 430 9. Sturm, C., Zhang, Q. & Noone, D. An introduction to stable water isotopes in climate models:  
431 benefits of forward proxy modelling for paleoclimatology, *Clim. Past*, **6**, 115--129. Preprint at  
432 (2010).
- 433 10. Gat, J. *Isotope Hydrology: A Study of the Water Cycle*. vol. 6 (Imperial College Press, 2010).

- 434 11. Bowen, G. J., Cai, Z., Fiorella, R. P. & Putman, A. L. Isotopes in the Water Cycle: Regional- to  
435 Global-Scale Patterns and Applications. *Annu. Rev. Earth Planet. Sci.* **47**, 453–479 (2019).
- 436 12. Dansgaard, W. Stable isotopes in precipitation. *Tellus* **16**, 436–468 (1964).
- 437 13. Craig, H. & Gordon, L. I. Deuterium and oxygen 18 variations in the ocean and the marine  
438 atmosphere. in *Stable Isotopes in Oceanographic Studies and Paleotemperatures* (ed. Tongiorgi, E.)  
439 9–130 (Consiglio Nazionale Delle Ricerche, Laboratorio di Geologia Nucleare - Pisa, 1965).
- 440 14. Rohling, E. J. PALEOCEANOGRAPHY, PHYSICAL AND CHEMICAL PROXIES | Oxygen  
441 Isotope Composition of Seawater. in *Encyclopedia of Quaternary Science (Second Edition)* (eds.  
442 Elias, S. A. & Mock, C. J.) 915–922 (Elsevier, 2013).
- 443 15. Konecky, B. L. *et al.* The Iso2k database: a global compilation of paleo- $\delta^{18}\text{O}$  and  $\delta^2\text{H}$  records to aid  
444 understanding of Common Era climate. *Earth Syst. Sci. Data* **12**, 2261–2288 (2020).
- 445 16. Urey, H. C. Oxygen isotopes in nature and in the laboratory. *Science* **108**, 489–496 (1948).
- 446 17. Kaufman, D. *et al.* Holocene global mean surface temperature, a multi-method reconstruction  
447 approach. *Sci Data* **7**, 201 (2020).
- 448 18. Brady, E. *et al.* The Connected Isotopic Water Cycle in the Community Earth System Model  
449 Version 1. *Journal of Advances in Modeling Earth Systems* vol. 11 2547–2566 Preprint at  
450 <https://doi.org/10.1029/2019ms001663> (2019).
- 451 19. Stevenson, S. *et al.* Volcanic Eruption Signatures in the Isotope-Enabled Last Millennium Ensemble.  
452 *Paleoceanography and Paleoclimatology* **34**, 1534–1552 (2019).
- 453 20. Otto-Bliesner, B. L. *et al.* Climate Variability and Change since 850 CE: An Ensemble Approach  
454 with the Community Earth System Model. *Bull. Am. Meteorol. Soc.* **97**, 735–754 (2016).
- 455 21. Thompson, D. M. *et al.* Identifying hydro-sensitive coral  $\delta^{18}\text{O}$  records for improved high-resolution  
456 temperature and salinity reconstructions. *Geophys. Res. Lett.* **49**, (2022).
- 457 22. Rozanski, K., Araguás-Araguás, L. & Gonfiantini, R. Isotopic patterns in modern global  
458 precipitation. in *Climate Change in Continental Isotopic Records* (eds. Stewart, P. K., Lohmann, K.  
459 C., McKenzie, J. & Savin, S.) vol. 78 1–36 (American Geophysical Union, 1993).

- 460 23. Petit, J. R. *et al.* Climate and atmospheric history of the past 420,000 years from the Vostok ice core,  
461 Antarctica. *Nature* **399**, 429–436 (1999).
- 462 24. Guan, J. *et al.* Understanding the temporal slope of the temperature-water isotope relation during the  
463 deglaciation using isoCAM3: The slope equation. *J. Geophys. Res.* **121**, (2016).
- 464 25. Siler, N. *et al.* The large-scale, long-term coupling of temperature, hydrology, and water isotopes. *J.*  
465 *Clim.* 1–51 (2021).
- 466 26. Falster, G., Konecky, B., Madhavan, M., Stevenson, S. & Coats, S. Imprint of the Pacific Walker  
467 Circulation in Global Precipitation  $\delta^{18}\text{O}$ . *J. Clim.* **34**, 8579–8597 (2021).
- 468 27. Putman, A. L., Bowen, G. J. & Strong, C. Local and regional modes of hydroclimatic change  
469 expressed in modern multidecadal precipitation oxygen isotope trends. *Geophys. Res. Lett.* **48**,  
470 (2021).
- 471 28. Majoube, M. Fractionnement en oxygene 18 et en deuterium entre l'eau et sa vapeur. *Journal de*  
472 *Chimie Physique* **68**, 1423–1436 (1971).
- 473 29. Craig, H., Gordon, L. I. & Horibe, Y. Isotopic exchange effects in the evaporation of water: 1. Low-  
474 temperature experimental results. *J. Geophys. Res. C: Oceans* **68**, 5079–5087 (1963).
- 475 30. Horita, J., Rozanski, K. & Cohen, S. Isotope effects in the evaporation of water: a status report of the  
476 Craig-Gordon model. *Isotopes Environ. Health Stud.* **44**, 23–49 (2008).
- 477 31. Nusbaumer, J., Wong, T. E., Bardeen, C. & Noone, D. Evaluating hydrological processes in the  
478 Community Atmosphere Model Version 5 (CAM5) using stable isotope ratios of water. *J. Adv.*  
479 *Model. Earth Syst.* **9**, 949–977 (2017).
- 480 32. Aggarwal, P. K. *et al.* Stable isotopes in global precipitation: A unified interpretation based on  
481 atmospheric moisture residence time. *Geophys. Res. Lett.* **39**, L11705 (2012).
- 482 33. Held, I. M. & Soden, B. J. Robust responses of the hydrological cycle to global warming. *J. Clim.*  
483 **19**, 5686–5699 (2006).
- 484 34. Gat, J. R., Mook, W. G. & Meijer, H. A. *Environmental Isotopes in the Hydrological Cycle, 2nd ed.*  
485 vol. 2 (International Atomic Energy Agency, Vienna, Austria, 2001).

- 486 35. Bailey, A., Posmentier, E. & Feng, X. Patterns of evaporation and precipitation drive global isotopic  
487 changes in atmospheric moisture. *Geophys. Res. Lett.* **45**, 7093–7101 (2018).
- 488 36. Neukom, R., Steiger, N., Gómez-Navarro, J. J., Wang, J. & Werner, J. P. No evidence for globally  
489 coherent warm and cold periods over the preindustrial Common Era. *Nature* **571**, 550–554 (2019).
- 490 37. Stuiver, M., Grootes, P. M. & Braziunas, T. F. The GISP2  $\delta^{18}\text{O}$  Climate Record of the Past 16,500  
491 Years and the Role of the Sun, Ocean, and Volcanoes. *Quat. Res.* **44**, 341–354 (1995).
- 492 38. Vuille, M. *et al.* A review of the South American Monsoon history as recorded in stable isotopic  
493 proxies over the past two millennia. *Clim. Past* **8**, 1309–1321 (2012).
- 494 39. Zhao, K. *et al.* A high-resolved record of the Asian Summer Monsoon from Dongge Cave, China for  
495 the past 1200 years. *Quat. Sci. Rev.* **122**, 250–257 (2015).
- 496 40. Konecky, B. L. *et al.* Intensification of southwestern Indonesian rainfall over the past millennium.  
497 *Geophys. Res. Lett.* **40**, 386–391 (2013).
- 498 41. Cook, E. R., Seager, R., Cane, M. A. & Stahle, D. W. North American drought: Reconstructions,  
499 causes, and consequences. *Earth-Sci. Rev.* **81**, 93–134 (2007).
- 500 42. Shuman, B. N. *et al.* Placing the Common Era in a Holocene context: millennial to centennial  
501 patterns and trends in the hydroclimate of North America over the past 2000 years. *Clim. Past* **14**,  
502 665–686 (2018).
- 503 43. Li, J., Xie, S.-P. & Cook, E. R. El Niño phases embedded in Asian and North American drought  
504 reconstructions. *Quat. Sci. Rev.* **85**, 20–34 (2014).
- 505 44. Bjerknes, J. Atmospheric teleconnections from the equatorial Pacific. *Mon. Weather Rev.* **97**, 163–  
506 172 (1969).
- 507 45. Kong, W. & Chiang, J. C. H. Southward shift of westerlies intensifies the east Asian early summer  
508 rainband following El Niño. *Geophys. Res. Lett.* **47**, (2020).
- 509 46. Seager, R. *et al.* Adjustment of the atmospheric circulation to tropical Pacific SST anomalies:  
510 Variability of transient eddy propagation in the Pacific-North America sector. *Quart. J. Roy. Meteor.*  
511 *Soc.* **136**, 277–296 (2010).

- 512 47. Wittenberg, A. T. Are historical records sufficient to constrain ENSO simulations? *Geophys. Res.*  
513 *Lett.* **36**, L12702 (2009).
- 514 48. Collins, M. *et al.* The impact of global warming on the tropical Pacific Ocean and El Niño. *Nat.*  
515 *Geosci.* **3**, 391–397 (2010).
- 516 49. Vecchi, G. *et al.* Weakening of tropical Pacific atmospheric circulation due to anthropogenic forcing.  
517 *Nature* **441**, 73–76 (2006).
- 518 50. Falster, G., Konecky, B., Coats, S. & Stevenson, S. Forced changes in the Pacific Walker circulation  
519 over the past millennium. *Nature* (2023) doi:10.1038/s41586-023-06447-0.
- 520 51. Cheng, H. *et al.* Ice age terminations. *Science* **326**, 248–252 (2009).
- 521 52. Wang, Y. J. *et al.* A High-Resolution Absolute-Dated Late Pleistocene Monsoon Record from Hulu  
522 Cave, China. *Science* **294**, 2345–2348 (2001).
- 523 53. Dayem, K. E., Molnar, P., Battisti, D. S. & Roe, G. H. Lessons learned from oxygen isotopes in  
524 modern precipitation applied to interpretation of speleothem records of paleoclimate from eastern  
525 Asia. *Earth Planet. Sci. Lett.* **295**, 219–230 (2010).
- 526 54. Osman, M. B., Coats, S., Das, S. B., McConnell, J. R. & Chellman, N. North Atlantic jet stream  
527 projections in the context of the past 1,250 years. *Proc. Natl. Acad. Sci. U. S. A.* **118**, (2021).
- 528 55. Hendricks. Space and time variation of d18O and dD in precipitation: Can paleotemperature be  
529 estimated from ice cores? *Global Biogeochemical Cycles* (2000) doi:10.1029/1999GB001198.
- 530 56. Liu, Z. *et al.* Younger Dryas cooling and the Greenland climate response to CO<sub>2</sub>. *Proceedings of the*  
531 *National Academy of Sciences* **109**, 11101–11104 (2012).

532

533

534

## 535 **Methods**

### 536 **Disaggregation of analyses by isotope interpretation**



537 All global analyses presented in this paper are disaggregated by isotope interpretation rather than  
538 by the original authors' climatic interpretation. This approach avoids building into our synthesis  
539 *a priori* assumptions about the specific climatic variable driving  $\delta^{18}\text{O}$  and  $\delta^2\text{H}$  variability in each  
540 record, the basis for which is not always explained in the original publications. In addition, many  
541 records contain multiple climatic interpretations (e.g., speleothem  $\delta^{18}\text{O}$  being driven mainly by  
542 monsoonal rainfall amount, but amplified by the ratio of summer vs. winter moisture source  
543 changes<sup>51-53</sup>), and the relative importance of each variable was impossible to objectively evaluate  
544 for every time scale, region, and proxy system in the database. Finally, climatic interpretations of  
545 isotope-based proxy records are continually evolving as new information emerges from  
546 environmental monitoring and modeling studies (e.g., moisture source and transport  
547 characteristics driving Greenland ice core  $\delta^{18}\text{O}$  variability<sup>25,35,54-56</sup>; seawater  $\delta^{18}\text{O}$  driving coral  
548  $\delta^{18}\text{O}$  in some regions<sup>21</sup>). The isotope interpretation groupings are less subject to interpretation  
549 because they chiefly represent isotope systematics and the physical pools of environmental  
550 waters that each proxy sensor imbibes.

551  
552 We separated  $\delta_{\text{precip}}$  and EM records because EM proxies integrate information about evaporation  
553 that is not expected from pure  $\delta_{\text{precip}}$  proxies, which are mainly driven by factors influencing  
554 condensation (e.g. air temperature, degree of rainout, import of moisture from different  
555 sources)<sup>7,11</sup>.

556

### 557 **Calculation of $\Delta^{18}\text{O}$ composites**

558 All records were extracted from the PAGES Iso2k Database v 1.0.0<sup>15,57</sup>. The database contains  
559 metadata on the principal determinants of isotopic composition in the measured material (e.g.,

560 the  $\delta^{18}\text{O}$  of precipitation that forms glacial ice or cave dripwaters) and the record's climatic  
561 interpretation (e.g., atmospheric temperature at condensation level, rainout due to monsoon  
562 intensity), as interpreted by the original studies' authors and our team of archive experts<sup>15</sup>. For  
563 each isotope interpretation group, we calculated an ensemble of 100 composite  $\delta^{18}\text{O}$  time series  
564 for the CE. Prior to calculation, we filtered the database to only include the 'primary' time series  
565 for each site, and then grouped records according to the primary driver of isotopic variability i.e.,  
566 EM, temperature, or  $\delta_{\text{precip}}$ <sup>15,57</sup>) (entitled 'EffectiveMoisture', 'Temperature', and 'P\_isotope' in  
567 the 'isotopeInterpretation1\_variableGroup' metadata field of the Iso2k database).

568

569 For records with isotope interpretation 'P\_isotope', we also calculated separate composites for a)  
570 glacier ice only, and b) excluding glacier ice (Extended Data Fig. 1). This separation was  
571 performed to assess whether composite  $\Delta^{18}\text{O}_{\delta_{\text{precip}}}$  is overprinted by the large number of ice core  
572 records from high latitudes and high elevations, where temperature-driven isotopic fractionation  
573 may disproportionately affect  $\delta_{\text{MW}}$ <sup>2</sup>. An especially strong temperature- $\delta_{\text{MW}}$  relationship may be  
574 unsurprising in the glacier ice  $\delta^{18}\text{O}$  system. Glacier ice reflects  $\delta_{\text{precip}}$  more directly than other  
575 proxy sensors, which reflect pools of meteoric water (e.g. soil water and lake water) that are  
576 influenced by precipitation and other secondary processes such as evaporation or aquifer  
577 mixing. Glacier ice is found at high latitudes and altitudes, where cold temperatures drive  
578 stronger stable isotope fractionation due to Rayleigh distillation and global patterns of  
579 precipitation vs. evaporative recharge<sup>10–12,22,23,25,35,55</sup>. Most of the glacier ice records included in  
580 the Iso2k database are consistently interpreted as temperature indicators, and were included in  
581 the PAGES 2k<sup>1,2</sup> temperature database used for GMST calculations.

582

583 Despite these considerations, the observed global  $\delta_{MW}$ -temperature relationship persists even  
584 when glacier ice records are removed from the  $\delta_{precip}$  composite (**Extended Data Fig. 1**), and in  
585 low- and mid-latitudes where local temperature effects on  $\delta_{precip}$  are small<sup>12</sup> (**Fig. 2**). The overall  
586 patterns in PC1 are also similar regardless of whether glacier ice records are included or  
587 excluded (**Extended Data Figs. 3, 8**). Therefore, the inclusion or exclusion of glacier ice records  
588 does not substantially affect the composites or PCA, supporting that the strong temperature- $\delta_{MW}$   
589 relationship in our data is due to the overall influence of temperature on the global pool of  
590 meteoric water and not due to the strong effect of air temperature on high-latitude ice cores.

591  
592 Records with ten or fewer data values within the CE were excluded from the analysis.  $\delta^2H$   
593 records (n=45 in composite  $\Delta^{18}O_{\delta_{precip}}$ , n=12 in composite  $\Delta^{18}O_{EM}$ ) were divided by eight to  
594 scale the magnitude of their variance with that of  $\delta^{18}O$  in global meteoric waters<sup>58</sup>. This was  
595 done to avoid erroneously high apparent climate variability at  $\delta^2H$  sites simply from the eight-  
596 times-higher variability in  $\delta^2H$  relative to  $\delta^{18}O$ , which arises from relative differences in  
597 equilibrium fractionation factors between liquid and vapor for these isotope ratios<sup>58</sup>. Local slopes  
598 were not available for the 12 records from evaporative water bodies in composite  $\Delta^{18}O_{EM}$ , so the  
599 global scaling of 8 was used.

600  
601 Records in the Iso2k database have a wide variety of temporal resolution, length, and coverage  
602 over the CE<sup>15</sup>. To align records to a common interval and resolution, the data were averaged into  
603 equal bins of 30 years spanning the CE, which approximates the average resolution of the lower  
604 resolution archive types in the database (marine and lake sediments). Records contributing to  
605 each bin were mean-centered but not scaled by variance, as described below. To minimize

606 aliasing, the data were binned following a modified nearest-neighbor annual interpolation  
607 procedure<sup>17</sup>. This approach accounts for the fact that for the non-annually-resolved data, the age  
608 of a sample at a given depth typically represents more than one year of accumulation (and up to  
609 several years or decades, or even longer for some low-resolution sedimentary records), and may  
610 therefore contain climate information that is relevant to more than one bin. The duration of each  
611 sample is not consistently recorded in the Iso2k database (or the primary references), so to  
612 estimate sample coverage we calculated the distribution of gaps between adjacent observations in  
613 each timeseries, and used nearest-neighbor interpolation to estimate sample values spanning the  
614 intervals that are less than the 75th quantile of the distribution of all gaps between adjacent  
615 observations (consistent with Kaufman et al.<sup>17</sup>). Consequently, samples with resolution <30  
616 years can potentially contribute to the weighted  $\delta^{18}\text{O}$  calculation for up to two bins, though with  
617 less weight given to samples further from their published age. In the case of records with  
618 resolution >30 years, this data-spreading step allows observations to impact the composites  
619 across multiple bins, consistent with their interpretation as multidecadal averages.

620

621 Record lengths also vary widely in the database, so there is no universal time period of common  
622 overlap within the CE. We therefore aligned the records using the Dynamic Compositing  
623 approach<sup>17</sup>, which uses randomly selected portions of each time series to adjust the  $\delta^{18}\text{O}$   
624 variance, then iteratively adjusts the mean  $\delta^{18}\text{O}$  of each time series so that the mean of each  
625 record is minimally offset from all other records in the composite. This process was repeated for  
626 each of 100 ensemble members. Because the mean value of the records is adjusted during  
627 compositing, the composite values are now in relative  $\Delta^{18}\text{O}$  (in ‰), rather than in their original  
628  $\delta^{18}\text{O}$  (or pre-scaled  $\delta^2\text{H}$ ) values on the VSMOW-SLAP scale (i.e., in  $1000 \cdot \delta$  notation where 0‰

629 refers to standard mean ocean water). Therefore, for convenience, composite  $\Delta^{18}\text{O}$  was slightly  
630 shifted such that the mean of the ensemble median is 0‰. The final composite  $\Delta^{18}\text{O}$  values (**Fig.**  
631 **1**) are therefore in units of ‰ anomalies relative to the 2000-year mean. Dynamic compositing  
632 was used in ref. <sup>17</sup> to produce calibrated reconstructions of paleotemperature. Unlike surface air  
633 temperature observations, long and complete timeseries of globally distributed  $\delta_{\text{precip}}$ ,  $\delta_{\text{MW}}$ , and  
634  $\delta_{\text{sw}}$  observations are insufficient (e.g. for  $\delta_{\text{precip}}$ , large spatial coverage gaps and few records  
635 longer than 10 years<sup>26</sup>), and so calibrated reconstructions are not possible until these  
636 observational networks are improved.

637

638

639

#### 640 **PCA of Iso2k data**

641 We used PCA to calculate Empirical Orthogonal Functions (EOFs) from a subset of records in  
642 the Iso2k database that met requirements for temporal coverage (described below; Fig. 2). Prior  
643 to calculating the EOFs, we filtered the database as described for the  $\Delta^{18}\text{O}$  composites, and  
644 binned the raw data. PCA was performed using records in each of the three “isotope  
645 interpretation” categories; for ‘P\_isotope’ records, we performed separate PCA for a) glacier  
646 ice, and b) ‘not glacier ice’ (i.e., all P\_isotope records that are not from glacier ice). PCA was  
647 performed on three temporal subsets: 0-1980 CE (30-year bins), 850-1840 (30-year bins), and  
648 1850-2005 (3-year bins). Here we describe the methodology for the 850-1840 PCA that is shown  
649 in the main text, then outline any adaptations that were made for the other two intervals.

650

651 Prior to PCA, all records were truncated to a fixed time interval of 850-1840. Other time  
652 windows were explored and are presented in Extended Data Figs. 3 and 8. The 850-1840 interval  
653 was chosen in order to focus on pre-industrial variability, to avoid issues with records or  
654 chronologies not extending fully to either the present day or the start of the CE, and to provide  
655 comparison with LM model experiments from 850-1850. (Note a 990-year interval was used  
656 because it is divisible by the 30-year bin size). Results of PCA on the 0-1980 interval (with 30-  
657 year bins) and 1850-2005 (with 3-year bins) are shown in Extended Data Figs. 3 and 8. All data  
658 processing for these intervals was as below.

659

660 Records included in the PCA had to meet stricter time coverage and completeness requirements  
661 than records included in the composites. Binned records with <85% temporal coverage during  
662 the 850-1840 interval were excluded. EOF analysis was carried out on the matrix of remaining,  
663 screened time series using the Data Interpolation Empirical Orthogonal Function (DINEOF)  
664 method, which accounts for records with a small number of missing data points<sup>59,60</sup>. DINEOF  
665 performs best when missing values are scattered randomly throughout the input data time series.  
666 In the case of Iso2k records, missing data are generally concentrated at the ends of records, and  
667 hence records with a large proportion of missing data have a large impact on the PC loadings  
668 (though less impact on the overall PC time series). To check for obvious artifacts induced by the  
669 data processing, we visually compared the binned and interpolated records with their raw data  
670 equivalents. We performed the PCA on the binned and interpolated data matrix using the `rda()`  
671 function of the ‘vegan’ package in R<sup>61</sup>. We scaled the interpolated records to unit variance  
672 because they are from different proxy systems and hence the raw data have widely ranging  
673 variance.

674

675 To test whether variability explained by the principal components could be explained  
676 stochastically, we tested the magnitude of the eigenvalues against a stochastic null hypothesis,  
677 using a block bootstrap method that accounts for decadal persistence (Extended Data Fig. 9). For  
678 the 850-1840 analysis, we split all raw data records that contributed to the EOF into ten-year  
679 blocks; we chose ten years because this separates interannual variance from interdecadal  
680 persistence. For each time series, we randomly selected an initial block, identified all blocks with  
681 similar means, and randomly sampled one block from these. The next selected block was the  
682 successor to that randomly sampled block. Blocks with similar means were identified using  
683 nearest neighbor-based ranking. For blocks with no successor (i.e., where there is a gap in the  
684 time series), the successor block was randomly selected from all other blocks. The process was  
685 then repeated 1000 times to produce an ensemble of time series. This method of re-sampling  
686 preserves the effects of 1) irregular time spacing, 2) the autocorrelation function (to lags >30  
687 years), and 3) the time series processing steps (e.g., binning) on the correlation structure of the  
688 raw (unprocessed) time series. We followed exactly the same steps for the 0-1980 PCA, using a  
689 30-year bin size.

690

691 The 1850-2004 PCA was performed using three-year bins, on records with 80% coverage. Block  
692 bootstrap was performed using 3-year blocks because 10-year blocks were too coarse for this  
693 short time period. As with the above, records were binned and standardized but not detrended.

694

695 **PCA with iCESM experiments**

696 To compare the iCESM with Iso2k results, we performed PCA of 30-year binned iCESM surface  
697 soil water  $\delta^{18}\text{O}$  ( $\delta^{18}\text{O}_{\text{soil}}$ ) i.e. the model variable most comparable to evaporation-sensitive  
698 systems such as lakes. We used data from Iso2k EM site locations, spanning 850-1850, and then  
699 regressed the ensemble-mean first PC against model SLP. The binned  $\delta^{18}\text{O}_{\text{soil}}$  was calculated for  
700 gridpoint time series corresponding to the “effective moisture” sites, taken from each isotope-  
701 enabled Last Millennium Ensemble full-forcing ensemble member from the upper 0-10 cm of the  
702 soil profile in iCLM, then averaged to produce an ensemble mean. The upper 10 cm were chosen  
703 because in the model, isotopic fractionation is clearest at this level whereas  $\delta^{18}\text{O}_{\text{soil}}$  of deeper soil  
704 layers rapidly approaches  $\delta^{18}\text{O}_{\text{precip}}$ <sup>18,62</sup>. EOF analysis was performed using  $\delta^{18}\text{O}_{\text{soil}}$  because the  
705 “lake” land cover type in iCLM4 is non-fractionating<sup>18,62</sup> and hence no model variable is  
706 available for direct comparison with the large number of lake-based Iso2k  $\delta^{18}\text{O}_{\text{EM}}$  proxies. Yet to  
707 first order,  $\delta^{18}\text{O}_{\text{soil}}$  is similarly controlled by both  $\delta^{18}\text{O}_{\text{precip}}$  and surface evaporation, and  $\delta^{18}\text{O}_{\text{soil}}$   
708 is also an adequate comparison to tree cellulose and speleothem records in the Iso2k EM  
709 category.

710

### 711 **Correlations with sea level pressure and calculation of PWC index**

712 Observed SLP and  $\Delta\text{SLP}$  for the correlations against Iso2k HP PC1 (Fig. 4) were taken from the  
713 HadSLP2r dataset<sup>63</sup>. Following the treatment of the Iso2k data, the HadSLP dataset was binned  
714 to 3 years but not detrended or deseasonalized (Fig. 4).

715

716 The index for the trans-Pacific SLP gradient ( $\Delta\text{SLP}$ ) is defined as anomalies (from the monthly  
717 climatology) in the difference between area-mean SLP over the central-eastern Pacific Ocean  
718 ( $160^\circ\text{W}$ - $180^\circ\text{W}$ ,  $5^\circ\text{S}$ - $5^\circ\text{N}$ ) and the western Pacific and eastern Indian Oceans ( $80^\circ\text{E}$ - $160^\circ\text{E}$ ,  $5^\circ\text{S}$ -



719 5°N)<sup>49</sup>. Positive  $\Delta$ SLP values represent an increased zonal pressure gradient, and hence stronger  
720 PWC (and vice versa).  $\Delta$ SLP was calculated using HadSLP2r for comparisons with Iso2k (Fig.  
721 4).

722

### 723 **Magnitudes of change in composite $\Delta^{18}\text{O}$ and GMST**

724 To estimate the magnitude of change in the three composite  $\Delta^{18}\text{O}$  time series, we subtracted the  
725 composite  $\Delta^{18}\text{O}$  value at 1000 CE from the composite  $\Delta^{18}\text{O}$  value at 1850 CE, for all 100  
726 composite ensemble members. We likewise calculated the difference between 2000 CE and 1850  
727 CE. Similarly for estimating the change in GMST during this interval, we subtracted the  
728 temperature anomaly at 1000 (1850) from the same at 1850 (2000), for all 7000 ensemble  
729 members. In all cases, we report the mean and standard deviation of the distributions of  
730 magnitudes of change.

731

### 732 **Calculation of isotope-temperature relationships in Iso2k data and iCESM experiments**

733 We calculated the relationship between composite  $\Delta^{18}\text{O}_{\delta_{\text{precip}}}$  (i.e., an approximation of  
734 anomalies in the global mean  $\delta^{18}\text{O}$  of precipitation, given the spatial distribution of 305  
735  $\delta_{\text{precip}}$ -sensitive proxy records) and GMST between 850-2000. We binned all ensemble  
736 members from the most recent reconstruction of CE GMST<sup>1</sup> to match the  $\Delta^{18}\text{O}_{\delta_{\text{precip}}}$   
737 composite. We then calculated linear regressions for 10000 unique combinations of  
738 composite  $\Delta^{18}\text{O}_{\delta_{\text{precip}}}$  ensemble member ( $n = 100$ ) on GMST ensemble member ( $n = 7000$ ),  
739 for the two time intervals. We report the mean and standard deviation of the distribution of  
740 regression coefficients, for the two time intervals.

741

742 For iCESM, isotope/temperature relationships were calculated for 850-2000 (the period of  
743 overlap with Iso2k composites) using area-weighted globally averaged, mean annual  
744 surface temperature and area-weighted, amount-weighted, mean annual global average  
745  $\delta^{18}\text{O}_{\text{precip}}$  from the ensemble-mean of three isotope-enabled Last Millennium Ensemble  
746 full-forcing simulations. Before determining the regression slopes, we calculated 30-year  
747 running means for both surface temperature and  $\delta^{18}\text{O}_{\text{precip}}$  (Fig. 3). Regression slopes in the  
748 main text are reported for GMST vs. two time series: global mean  $\delta^{18}\text{O}_{\text{precip}}$  (using all grid  
749 cells), and mean  $\delta^{18}\text{O}_{\text{precip}}$  calculated only for grid cells containing locations of Iso2k  
750 primary time series data contributing to the composites between 850-2000 CE.

751

752 Similarly, to estimate the amount of variance in individual Iso2k primary time series explained  
753 by proxy estimates of global temperature (Extended Data Fig. 6), we calculated  $R^2$  for the 30-  
754 year binned data across the interval 1-2000, ignoring bins that contained no observations.  
755 Correlations were only calculated if at least six bins overlapped the bins from the GMST  
756 reconstruction.

757

### 758 **Calculation of Relative Humidity normalized to SST**

759 Relative humidity was calculated from iCESM experiments for all grid points over the oceans  
760 from 60°N-60°S, i.e. the portion of the lower troposphere receiving the majority of evaporated  
761 water from the surface oceans.  $\text{RH}_{\text{SST}}$  in Fig. 3 was calculated as the relative humidity of the  
762 surface-most model layer, normalized to the saturation vapor pressure at the temperature of the  
763 surface ocean rather than the air, following the physical principles of the Craig-Gordon model  
764 for an evaporating water body<sup>13,29,30</sup>. All global-mean time series in Fig. 3 are area-weighted.

765

766 **Calculation of trends**

767 Trends (Fig. 2) were calculated as the slope of the linear regression  
768 from 850–1840 for a subset of Iso2k records meeting the following  
769 criteria: 1) designated ‘primary time series’, 2) containing at least  
770 one data point in the first and last 50 years of the time interval; and  
771 3) containing at least 20 data points over the full time interval (i.e.,  
772  $\geq 50$  year average resolution). For iCESM data, trends were calculated  
773 as the slope of the linear regression for monthly data covering the  
774 850–1850 and 1850–2005 time intervals.

775

776 **200-year standardized anomalies**

777 We created standardized anomaly (‘z score’) maps to aid interpretation of temporal variability in  
778 the composite time series (Extended Data Fig. 7). Similarly to the analyses described above, we  
779 filtered the database to only include the ‘primary’ isotope ( $\delta^{18}\text{O}$  or  $\delta^2\text{H}$ ) time series for each site,  
780 and then grouped records according to the primary driver of isotopic variability. We then filtered  
781 this subset of data sets to only include records spanning  $>600$  years within the CE. We averaged  
782 those records into 200-year bins, and then calculated z-scores for each bin by subtracting the  
783 mean of all data points within the CE from the bin average, and then dividing by the standard  
784 deviation of all data points within the CE. We performed this analysis using both ‘odd’ (100,  
785 300, 500 etc.) and ‘even’ (200, 400, 600) centuries as bin centers and showed only the time  
786 periods relevant to the main text in Extended Data Fig. 7.

787

788 **Data Availability Statement**

789 The Iso2k Database<sup>57</sup> is available for download at <https://doi.org/10.25921/57j8-vs18> and is  
790 accessible via the NOAA/WDS Paleo Data landing page at  
791 <https://www.ncdc.noaa.gov/paleo/study/29593>. Composites and principal components datasets  
792 generated for this manuscript are available through NOAA/NCEI at ...

793

794 **Code Availability Statement**

795 Codes to reproduce the main results from this manuscript are available via Github  
796 <https://github.com/nickmckay/iso2kNatureGeoscience2023> and archived on Zenodo [insert](#)  
797 [Zenodo here](#).

798

799 **Methods-only References**

800

801 57.Konecky, B. L. & McKay, N. P. NOAA/WDS Paleoclimatology - The Iso2k Database. NOAA  
802 National Centers for Environmental Information. (2020) doi:10.25921/57j8-vs18.

803 58.Craig, H. Isotopic Variations in Meteoric Waters. *Science* **133**, 1702–1703 (1961).

804 59.Beckers, J.-M., Barth, A. & Alvera-Azcárate, A. DINEOF reconstruction of clouded images  
805 including error maps–application to the Sea-Surface Temperature around Corsican Island. *Ocean*  
806 *Science* **2**, 183–199 (2006).

807 60.Alvera-Azcárate, A., Barth, A., Sirjacobs, D., Lenartz, F. & Beckers, J.-M. Data Interpolating  
808 Empirical Orthogonal Functions (DINEOF): a tool for geophysical data analyses. *Mediterr. Mar.*  
809 *Sci.* **12**, 5–11 (2011).

810 61.Oksanen, J., Kindt, R., Legendre, P. & Others. Vegan: community ecology package. R package  
811 version 2.2-1. R Development Core Team, Vienna. Preprint at (2015).

812 62. Wong, T. E., Nusbaumer, J. & Noone, D. C. Evaluation of modeled land-atmosphere exchanges  
813 with a comprehensive water isotope fractionation scheme in version 4 of the Community Land  
814 Model. *J. Adv. Model. Earth Syst.* **9**, 978–1001 (2017).

815 63. Allan, R. & Ansell, T. A New Globally Complete Monthly Historical Gridded Mean Sea Level  
816 Pressure Dataset (HadSLP2): 1850–2004. *J. Clim.* **19**, 5816–5842 (2006).

817

818

819

**CAPTIONS FOR EXTENDED DATA FIGURES 1-9**

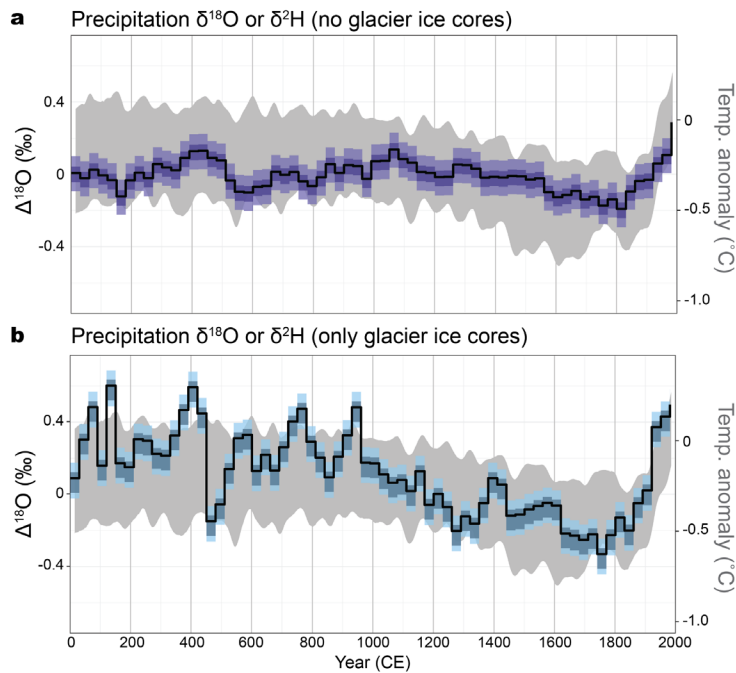
820

**THIS CONTENT WILL BE MOVED TO A SEPARATE DOCUMENT & FIGS WILL**

821

**BE DELETED AS PER EDITOR INSTRUCTIONS**

822



823

824 **Extended Data Figure 1. Composite  $\Delta^{18}\text{O}_{\delta\text{precip}}$  calculated with and without glacier ice**

825 **records.** As per Fig. 1, the black line with coloured shading shows the 30-year binned proxy

826  $\delta^{18}\text{O}$  anomaly from Iso2k records<sup>15</sup> (black line, ensemble median; dark shading, first and third

827 quantiles; light shading, 2.5th/97.5th percentiles). **(a)** Composite of  $\Delta^{18}\text{O}_{\delta\text{precip}}$  records from all

828 archives other than glacier ice. **(b)** Composite of only glacier ice records. Records contributing

829 to each bin are mean-centered but not scaled according to that record's variance (see Methods).

830 Anomalies are in ‰ relative to the 2000-year mean. Gray shading depicts the ensemble 2.5 and

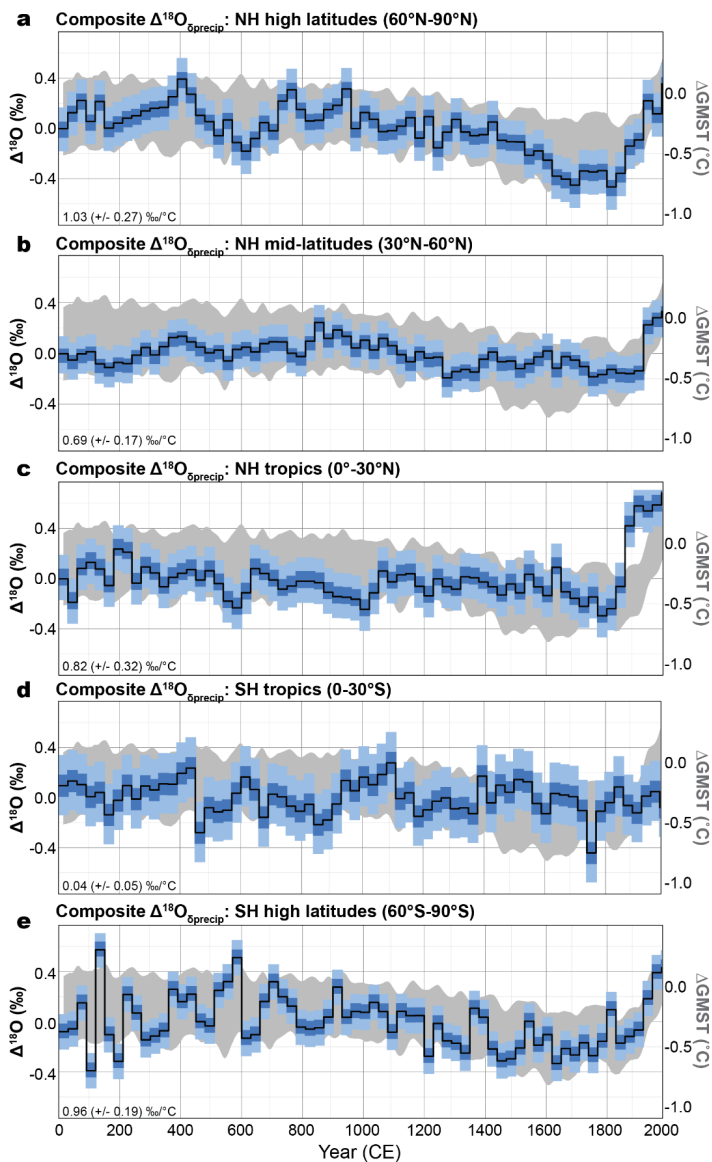
831 97.5 percentile of the 31-year Butterworth-filtered Global Mean Surface Temperature (GMST)

832 anomaly relative to the 1961-1990 mean<sup>1</sup>.

833

834

835



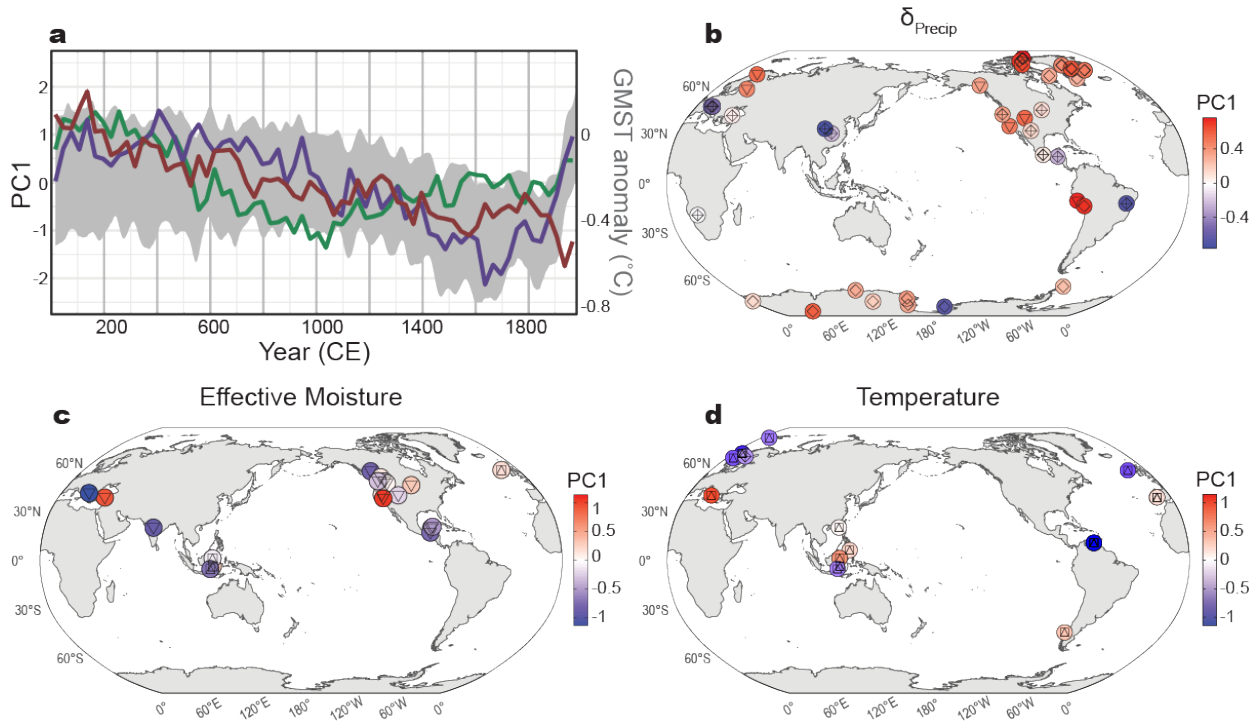
836

837 **Extended Data Figure 2. Composite  $\Delta^{18}\text{O}_{\delta\text{precip}}$  calculated using Iso2k records<sup>15</sup> falling**  
 838 **within 30-degree latitudinal bins. a, 60-90°N (n=76); b, 30-60°N (n=86); c, 0-30°N (n=27); d,**  
 839 **0-30°S (n=39); e, 60-90°S (n=77).** As per Fig. 1, black line with coloured shading shows the 30-  
 840 year binned proxy  $\delta^{18}\text{O}$  anomaly (black line, ensemble median; dark shading, first and third  
 841 quantiles; light shading, 2.5th/97.5th percentiles) and gray shading depicts the ensemble 2.5 and  
 842 97.5 percentile of the 31-year Butterworth-filtered GMST anomaly relative to the 1961-1990  
 843 mean<sup>1</sup>. Black text denotes mean regression slope ( $\pm 1$  standard deviation) of regional composite



844  $\Delta^{18}\text{O}$  vs. GMST from 850-2000. Regional composite for 30-60°S not calculated due to  
 845 insufficient number of records from those latitudes (n=2).

846

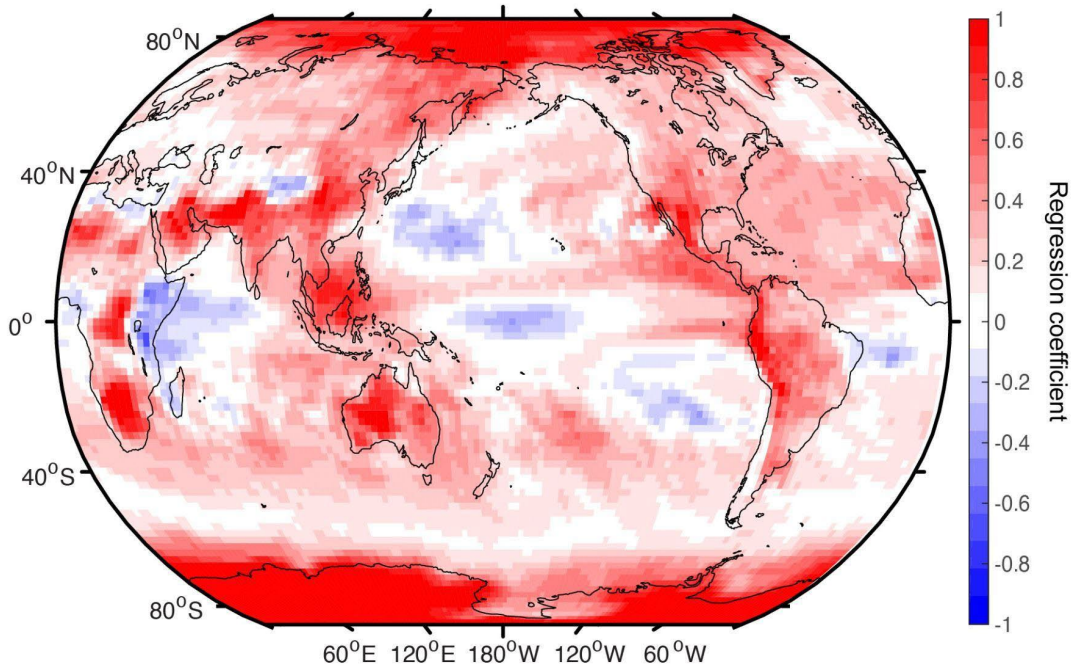


**Archive** (inner symbol):  $\diamond$  Ice  $\square$  Marine sediment  $\triangle$  Wood  $\nabla$  Lake sediment  $\diamond$  Speleothem  
 — Precipitation  $\delta^{18}\text{O}$  or  $\delta^2\text{H}$  ( $\delta_{\text{Precip}}$ ) — Effective Moisture — Temperature

847

848 **Extended Data Figure 3. First Principal Component (PC1) of Iso2k<sup>15</sup> records during the**  
 849 **full Common Era.** Symbols, lines, and shading are as in Fig. 2 but for the interval 0-1980 (30-  
 850 year bins), and without trends depicted (i.e. constant shape for outer symbols).  $\delta_{\text{precip}}$  PC1  
 851 explains 19% of the total variance (n = 44). Effective Moisture PC1 explains 19% of the total  
 852 variance (n = 19). Temperature PC1 explains 25% of the total variance (n = 19). Maps created in  
 853 R using coastlines from Natural Earth.

854



855

856 **Extended Data Figure 4. iCESM relationship between GMST and grid cell-level  $\delta^{18}\text{O}_{\text{precip}}$ .**

857 Shading depicts the regression coefficient in  $\text{‰}/^\circ\text{C}$  between mean annual, amount-weighted, 30-

858 year running mean  $\delta^{18}\text{O}_{\text{precip}}$  at every grid cell vs. 30-year running mean, area-weighted GMST

859 for the mean of 3 full-forcing, isotope-enabled Last Millennium Ensemble members<sup>18–20</sup>. Map

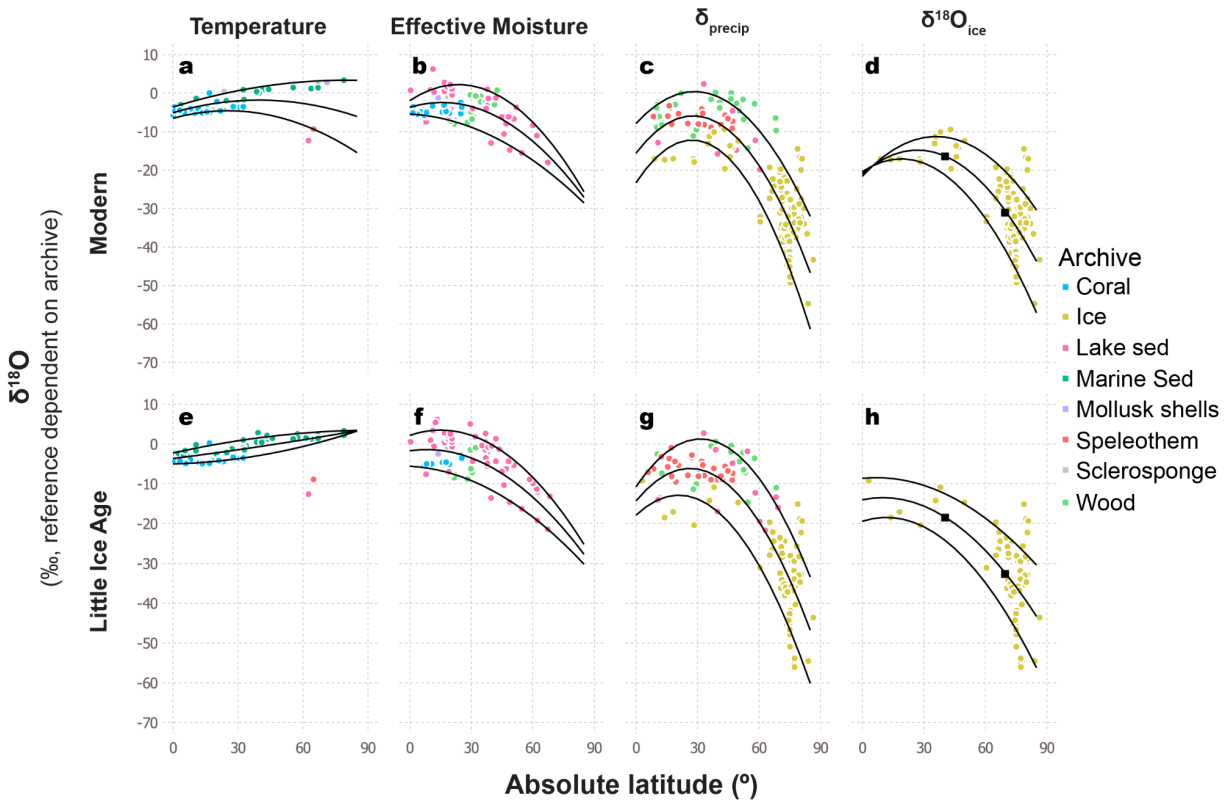
860 created in MATLAB using `m_map` for coastlines.

861

862

863

864



865

866 **Extended Data Figure 5.  $\delta^{18}\text{O}$  vs. latitude in the Iso2k database<sup>15</sup> for the modern era (a-d;**

867 **1950-2018) and the Little Ice Age (e-h; 1450-1850).** Data are plotted for the three main isotope

868 interpretation categories (a-c, e-g) and for  $\delta^{18}\text{O}$  of glacier and ground ice (d, h), the archives that

869 preserve precipitation most directly. Black lines indicate polynomial fits to the 0.1, 0.5, and 0.9

870 quantiles. Black squares on panels (d) and (h) indicate 40 and 70 degrees latitude, the interval for

871 which the mean of the gradient function was calculated ( $-0.48\text{‰}/^\circ$  latitude for both time periods;

872 see main text). All records are plotted in permil on the VSMOW-SLAP scale for ice core

873 records; PDB or VPDB for all other archives).

874

875

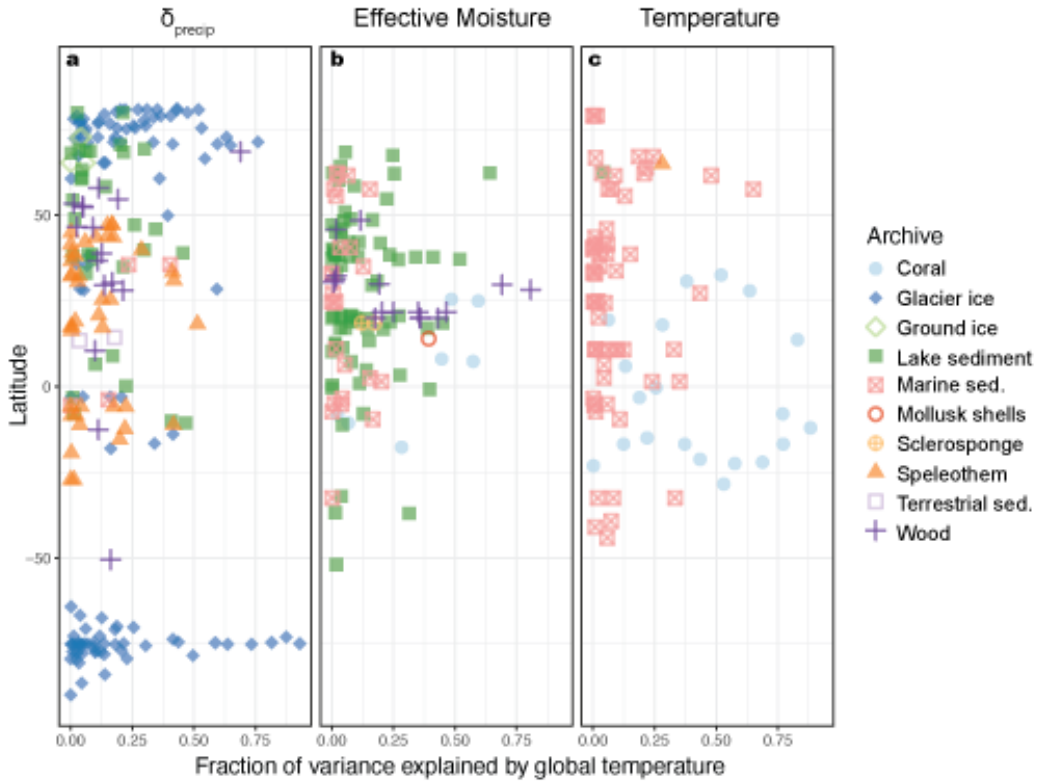
876

877

878

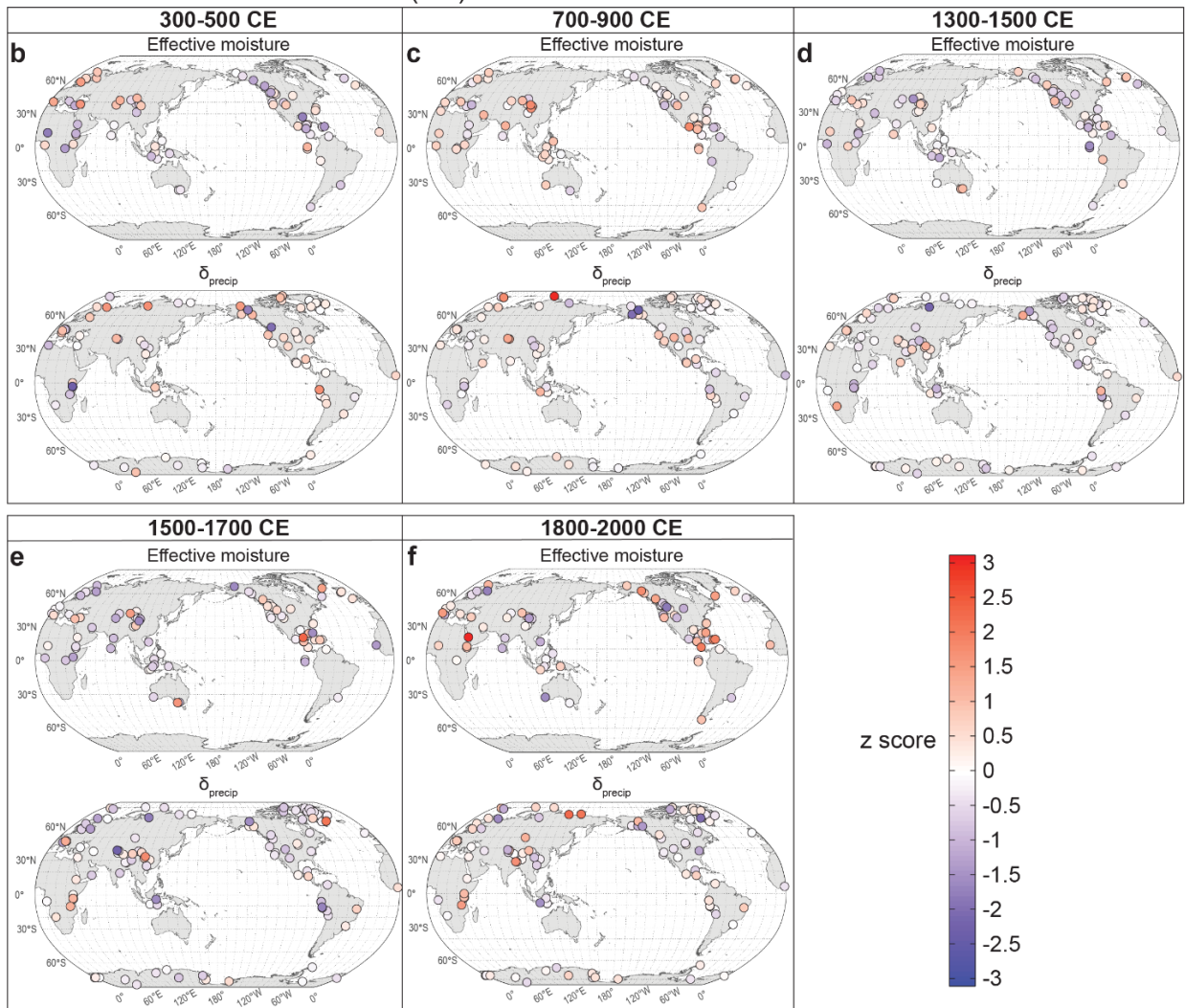
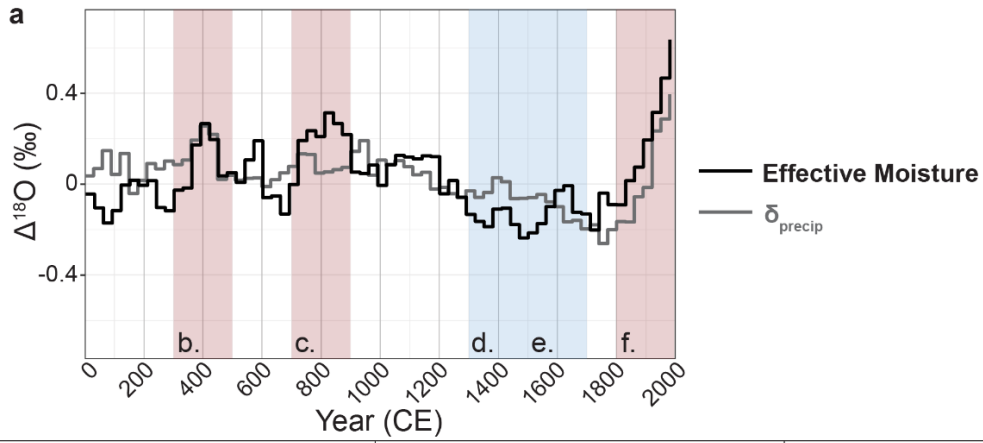
879

880



881  
 882 **Extended Data Figure 6. Relation between Iso2k<sup>15</sup> primary timeseries and Global Mean**  
 883 **Surface Temperature (GMST). (a)** Fraction of variance explained ( $R^2$ ) in  $\delta_{\text{precip}}$  primary time  
 884 series by changes in PAGES 2k global mean surface temperature (GMST) over the past 2000  
 885 years<sup>1,2</sup>. Both Iso2k time series and GMST were averaged into 30 year bins before calculating  
 886 correlations (See Methods). **(b)** As in (a), but for Effective Moisture primary time series. **(c)** As  
 887 in (a), but for Temperature primary time series.

888  
 889  
 890  
 891



893 **Extended Data Figure 7. Standardized 200-year  $\delta^{18}\text{O}$  anomalies from Effective Moisture**  
894 **and  $\delta_{\text{precip}}$  records. a,** Composite medians for Iso2k<sup>15</sup> Effective Moisture and  $\delta_{\text{precip}}$  driven  
895 records, as shown in Fig. 1 of the main text. Red shading denotes intervals of relatively high  
896 composite  $\Delta^{18}\text{O}_{\text{EM}}$ , and blue shading denotes intervals of relatively low composite  $\Delta^{18}\text{O}_{\text{EM}}$ . **b-f,**  
897 Isotopic anomalies in individual EM and  $\delta_{\text{precip}}$  records contributing to the  
898 composites during those shaded intervals, via standardised anomaly  
899 maps for time intervals discussed in the main text (see Methods).  
900 These maps only include records with data spanning  $\geq 600$  years.  
901 Standardized anomalies at each site are relative to the Common Era  
902 mean value for that record. Maps created in R using coastlines from  
903 Natural Earth.

904

905

906

907

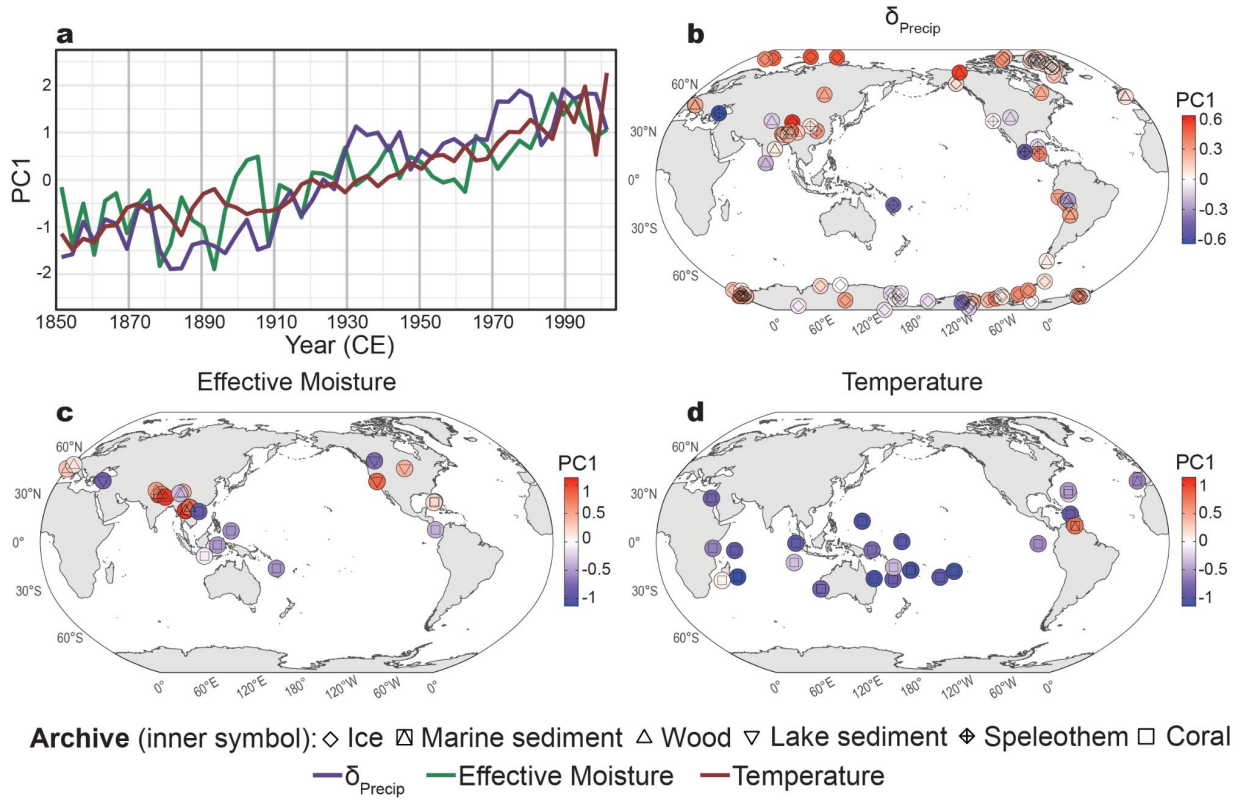
908

909

910

911

912  
 913  
 914  
 915  
 916  
 917  
 918  
 919  
 920  
 921  
 922

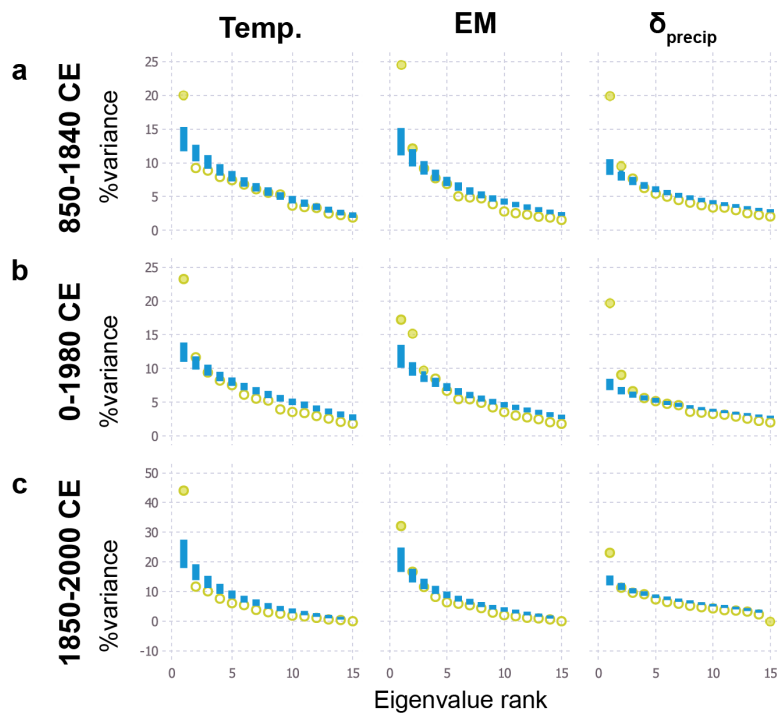


923  
 924



925 **Extended Data Figure 8. First Principal Component (PC1) of Iso2k<sup>15</sup> data for the Historical**  
 926 **Period.** Symbols, lines, and shading are as per Extended Data Fig. 3, but for the interval 1850-  
 927 2005, with 3-year bins.  $\delta_{\text{precip}}$  PC1 explains 12% of the total variance (n = 109). Effective  
 928 Moisture PC1 explains 32% of the total variance (n = 29). Temperature PC1 explains 38% of the  
 929 total variance (n = 27). Maps created in R using coastlines from Natural Earth.

930  
 931  
 932  
 933  
 934



935

936 **Extended Data Figure 9. Significance of Iso2k<sup>15</sup> PCA eigenvalues with respect to a null**  
937 **hypothesis of stochastic forcing with decadal persistence. a**, Block bootstrap results from 850-  
938 1840 with a 30-year bin width, 10-year block length, and tolerance of up to 15% missing data  
939 (i.e., 85% coverage during the time interval; Methods). Yellow symbols depict the eigenvalues  
940 (expressed as a percentage of the total variance) of each principal component. Blue bars show the  
941 1-99% confidence intervals of the stochastic null hypothesis (n=1000). Eigenvalues above the  
942 99% confidence interval are significant at the 1% level (one-sided test) and therefore are unlikely  
943 to have arisen stochastically, and unlikely to be an artifact of the data processing steps (i.e.,  
944 binning and interpolation). **(b)** as in **(a)** but for 0-1980. **(c)** as in **(a)** but for 1850-2000 and with a  
945 10-year bin width and tolerance of up to 10% missing data (90% coverage).

946

947

948

949